

# Ion pairing in model electrolytes: A study via three particle correlation functions

Felipe Jiménez-Ángeles,<sup>1,2,\*</sup> René Messina,<sup>3,†</sup>

Christian Holm,<sup>4,‡</sup> and Marcelo Lozada-Cassou<sup>1,2,§</sup>

<sup>1</sup>*Programa de Ingeniería Molecular, Instituto Mexicano del Petróleo,  
Lázaro Cárdenas 152, 07730 México D. F., México*

<sup>2</sup>*Departamento de Física, Universidad Autónoma Metropolitana-Iztapalapa,  
Apartado Postal 55-334, 09340 México D.F., México*

<sup>3</sup>*Institut für Theoretische Physik II,  
Heirich-Heine-Universität Düsseldorf,  
Universitätsstrasse 1, D-40225 Düsseldorf, Germany*

<sup>4</sup>*Max-Planck-Institut für Polymerforschung,  
Ackermannweg 10, 55128 Mainz, Germany*

(Dated: October 28, 2018)

## Abstract

A novel integral equations approach is applied for studying ion pairing in the restricted primitive model (RPM) electrolyte, i. e., the three point extension (TPE) to the Ornstein-Zernike integral equations. In the TPE approach, the three-particle correlation functions  $g^{[3]}(\mathbf{r}_1, \mathbf{r}_2, \mathbf{r}_3)$  are obtained. The TPE results are compared to molecular dynamics (MD) simulations and other theories. Good agreement between TPE and MD is observed for a wide range of parameters, particularly where standard integral equations theories fail, i. e., low salt concentration and high ionic valence. Our results support the formation of ion pairs and aligned ion complexes.

PACS numbers: 61.20.Qg

---

\*Electronic address: fangeles@www.imp.mx

†Electronic address: messina@mpip-mainz.mpg.de

‡Electronic address: holm@mpip-mainz.mpg.de

§Electronic address: marcelo@www.imp.mx

## I. INTRODUCTION

The restricted primitive model electrolyte (RPM) has been widely studied by means of integral equations [1, 2, 3, 4, 5, 6, 7, 8] and Monte Carlo (MC) simulations [9, 10]. All the approaches describe well the RPM in a wide regime of the fluid phase diagram. Nonetheless, they *all fail* in the dilute regime of a multivalent electrolyte [4, 7, 11], which can be relevant for the study of phase transitions in ionic fluids.

Such phase transition have been predicted as early as 1962, for ionic mixtures [12], and later for polyelectrolyte solutions [13]. Experiments for the gas-liquid phase transition of molten salts have been made in the past [14]. Among the first computer simulations of the RPM, where this transition is reported are those of Vorontsov-Vel'yaminov *et al.* [15, 16]. Recently, there has been a renewed interest in ionic phase transitions: Computer simulations studies for the RPM [17, 18, 19] and for variations of this model, where unsymmetrical ionic charge and size is considered [20, 21, 22, 23, 24, 25], have given insight into the nature of the phase transition and the molecular mechanisms behind these transitions. Experiments of a liquid-liquid phase transitions have also been reported [26, 27, 28, 29, 30]. Phase transitions of the RPM can be identified either with molten salts gas-liquid transition or with the two liquid transition, since in terms of dimensionless parameters the RPM does not distinguish between these two systems [31].

In the past, it has been proposed a powerful approach to systematically incorporate correlations into any given liquid theory [32, 33, 34, 35, 36, 37]. This method is known as *three point extension* (TPE) to integral equations. By construction, TPE explicitly provides valuable information of the three-particle correlations. In consequence, the resulting pair distribution function includes virtually infinitely more correlations and, hence, a better system description is expected. Although in the past TPE has not been applied to bulk fluids, our presumption is sustained by previous TPE calculation for inhomogeneous fluids where better agreement with computer simulations [38, 39, 40] were reported than in the case of *standard* [41] integral equation theories [34, 35].

In this paper we apply TPE to the RPM and compare with our molecular dynamics (MD) simulations. Based on *ion pairing association*, phase transitions in ionic fluids have been reported by computer simulations [24]. The results presented here, (both TPE and our MD) for this region of the phase diagram, support this ion paring association mechanisms.

Moreover, TPE, based on the agreement with our MD results, provides a reliable theory to study ionic fluids in the important phase diagram region of low ionic concentration and high coulombic coupling.

In spite of important theoretical efforts made in the past, a proper description of the full RPM electrolyte phase diagram is still required. Previous approaches to study triplet correlations have been developed by Kjellander *et al.* [42] and Plischke and Henderson [43, 44]. In their study, they considered a fluid next to a plate and they computed the inhomogeneous two-particle distribution function. More relevant for the present study, however, is that of Attard [45, 46], who calculated the two particle inhomogeneous distribution function (using the Percus-Yevick closure) for a hard sphere fluid next to a hard sphere particle. In his approach, he finds an excellent agreement with MC data. To the best of our knowledge, no triplet correlation function has been explicitly calculated for the RPM electrolyte.

In a study of the critical behavior of the RPM electrolyte at the level of the Debye-Hückel theory, Levin and Fisher [47, 48] have included triplet correlations by imposing the presence of ionic pairs, such a consideration reveals an Ising critical behavior. The ions pairs idea first proposed by Bjerrum [49] has been considerably extended by Levin and Fisher, Stell and co-workers [50, 51, 52, 53, 54] and Blum and co-workers [55, 56, 57, 58]. While ion pairing clearly seems to be the molecular mechanism ruling the ionic solutions phase transitions [18, 21, 24, 28, 59], its physical bases remain unexplained [24]. On the other hand, although in the past some experiments supported a classical critical behavior [28, 60], others the Ising universality class [61] and Singh and Pitzer [62] suggested a crossover from classical to Ising behavior, later experimental results, however, seem to agree in a crossover behavior [29, 30, 63, 64, 65]. Therefore, while ionic fluids asymptotic critical behavior appear to exhibit ultimately Ising-like critical behavior, the question of why do some ionic fluids appear to display classical behavior [47], remains unanswered [65]. A shortcoming of the ion pairing theories is that ion pairing is imposed and hence they provide an *ad hoc* molecular mechanism. Perhaps a better understanding of the molecular mechanisms behind phase transitions could be captured by a formal many body theory, such as TPE, where three particle correlations are calculated explicitly, and no ion pairing is imposed.

In this work, by using the TPE to integral equations approach, we obtain a better description of the RPM electrolyte: In particular for the strongly coupled region. We also analyze the formation of ion complexes. The structure of the article is set out as follows. In

Sec. II we present the TPE formalism. Section III is devoted to the computational details of the MD simulation. In Sec. IV, we present our results for two typical (divalent) electrolyte concentrations. The obtained three particle distribution function,  $g_{\beta\gamma i}^{[3]}(\mathbf{r}_1, \mathbf{r}_2, \mathbf{r}_3)$ , with TPE and MD simulation are compared and analyzed in terms of ion association. We also compare the mean force between two particles obtained with TPE, conventional HNC/MSA and MD. Finally, Sec. V contains concluding remarks.

## II. THEORY

### A. Three point extension to integral equation theories

The pair correlation function,  $g(\mathbf{r}_{12} \equiv \mathbf{r}_1 - \mathbf{r}_2)$ , of a one-component fluid with its components interacting through the pair potential  $u(\mathbf{r}_{12})$ , is related to the potential of mean force  $w(\mathbf{r}_{12})$  (between two particles located at  $\mathbf{r}_1$  and  $\mathbf{r}_2$ ) by

$$g(\mathbf{r}_{12}) = \exp\{-\beta w(\mathbf{r}_{12})\}. \quad (1)$$

If  $g(\mathbf{r}_{12})$  is expanded in powers of the bulk concentration, the  $n$ -th order coefficient is a sum of integrals of products of the Mayer function  $f(\mathbf{r}_{12}) \equiv \exp\{-\beta u(\mathbf{r}_{12})\} - 1$ . Such an integral of a product of Mayer functions can be conveniently represented by Mayer diagrams [37, 66, 67]. The diagrams of the first and second order coefficients are given in the left hand side of Fig. 1. There is still not an exact theory to compute  $g(\mathbf{r}_{12})$ , and all the available theories ignore several classes of topologically different diagrams. We will come back to this point below when we discuss the direct correlation function and the Ornstein-Zernike equation.

In a multi-component fluid, the total correlation function,  $h_{ij}(\mathbf{r}_{12}) \equiv g_{ij}(\mathbf{r}_{12}) - 1$ , between two particles of species  $i$  and  $j$  located at  $\mathbf{r}_1$  and  $\mathbf{r}_2$ , respectively, is related to the direct correlation function,  $c_{ij}(\mathbf{r}_{12})$ , through the Ornstein-Zernike equation which for a  $k$ -component fluid is given by

$$h_{ij}(\mathbf{r}_{12}) = c_{ij}(\mathbf{r}_{12}) + \sum_{m=1}^k \rho_m \int h_{im}(\mathbf{r}_{23}) c_{mj}(\mathbf{r}_{13}) d\mathbf{r}_3, \quad (2)$$

where  $\rho_m$  is the concentration of species  $m$ . Several closures between  $h_{ij}(\mathbf{r}_{12})$  and  $c_{ij}(\mathbf{r}_{12})$  have been proposed. For instance,

$$c_{ij}(\mathbf{r}_{12}) = -\beta u_{ij}(\mathbf{r}_{12}) + h_{ij}(\mathbf{r}_{12}) - \ln g_{ij}(\mathbf{r}_{12}), \quad (3)$$

$$c_{ij}(\mathbf{r}_{12}) = -\beta u_{ij}(\mathbf{r}_{12}), \quad \text{and} \quad (4)$$

$$c_{ij}(\mathbf{r}_{12}) = f_{ij}(\mathbf{r}_{12}) g_{ij}(\mathbf{r}_{12}) \exp\{\beta u_{ij}(\mathbf{r}_{12})\}. \quad (5)$$

Equations (3), (4) and (5) are known as the hypernetted chain equation (HNC), the mean spherical approximation (MSA) and the Percus-Yevick (PY) equation, respectively. In the hypernetted chain theory, the *bridge* diagrams are ignored whereas in the Percus-Yevick approximation both the bridge and *product* diagrams are neglected [66, 68]. The first and second order Mayer graphs of the HNC and PY theories are also given in Fig. 1.

Let us now propose [33, 37] that in a fluid of  $k$ -species there is an additional *dumbbell* species at infinite dilution made up of two particles (of species  $\beta$  and  $\gamma$ ) at *fixed* relative position  $\mathbf{t} \equiv \mathbf{r}_{12}$  (see Fig. 2). By defining the dumbbell species as  $\alpha$ , we now have a  $(k + 1)$ -component fluid. For  $\rho_\alpha \rightarrow 0$ , the total correlation function between the particle of species  $\alpha$  and the fluid particle of species  $j$  reads

$$h_{\alpha j}(\mathbf{r}_3) = c_{\alpha j}(\mathbf{r}_3) + \sum_{m=1}^k \rho_m \int h_{\alpha m}(\mathbf{r}_4) c_{mj}(\mathbf{r}_{34}) d\mathbf{r}_4, \quad (6)$$

where  $c_{mj}(\mathbf{r}_{34})$  is the direct correlation function between particles of species  $m$  and  $j$  both different from  $\alpha$ . In order to obtain  $c_{mj}(\mathbf{r}_{34})$ , the  $k$ -component Ornstein-Zernike equation [Eq. (2)] has to be used. Different integral equation theories [37] can be obtained depending on the closure relations used for  $c_{\alpha j}(\mathbf{r}_3)$  and  $c_{mj}(\mathbf{r}_{34})$  in Eq. (6). For instance, TPE-HNC/MSA is obtained if MSA [Eq. (4)] is used for  $c_{mj}(\mathbf{r}_{34})$  and HNC [Eq.(3)] for  $c_{\alpha i}(\mathbf{r}_3)$ .

In this formalism, the distribution function,  $g_{\alpha i}(\mathbf{r}_3)$ , of the  $i$  species around the  $\alpha$  species can be interpreted as a conditional three-particle distribution function denoted by  $g_{\beta\gamma i}^{[3]}(\mathbf{r}_3; \mathbf{t}) \equiv g_{\beta\gamma i}^{[3]}(\mathbf{r}_1, \mathbf{r}_2, \mathbf{r}_3; \mathbf{t} = \mathbf{r}_1 - \mathbf{r}_2)$ , i.e., the density probability of finding a particle of species  $i$  at  $\mathbf{r}_3$  in the presence of the dumbbell. Mathematically the conditional three particle distribution function,  $g_{\beta\gamma i}^{[3]}(\mathbf{r}_3; \mathbf{t})$ , is related to the homogeneous three particle distribution function  $g_{\beta\gamma i}^{(3)}(\mathbf{r}_1, \mathbf{r}_2, \mathbf{r}_3)$  by

$$g_{\beta\gamma i}^{[3]}(\mathbf{r}_3; \mathbf{t}) = \frac{g_{\beta\gamma i}^{(3)}(\mathbf{r}_1, \mathbf{r}_2, \mathbf{r}_3)}{g_{\beta\gamma}^{(2)}(\mathbf{t})}. \quad (7)$$

The projection of  $g_{\beta\gamma i}^{[3]}(\mathbf{r}_1, \mathbf{r}_2, \mathbf{r}_3)$  gives directly  $g_{\beta\gamma}^{(2)}(\mathbf{t})$ . This projection can be provided by the Born-Green-Yvon theorem (BGY) that is based on a balance of the mean effective force  $F_{\beta\gamma}[g_{\beta\gamma i}^{[3]}(\mathbf{r}_3; \mathbf{t})]$ .

### B. The Born-Green-Yvon equation or a force law

The Born-Green-Yvon (BGY) equation is one of the so called hierarchy equations and it is an exact theorem relating the  $n$  and  $(n + 1)$  particle distribution functions [69, 70]. Here, we derive the BGY equation as a sum of all the forces exerted on one of the two dumbbell's particles (let us say particle of species  $\gamma$  at  $\mathbf{r}_2$ ). This mean force has two contributions: (i) the direct force  $\mathbf{f}_{\beta\gamma}(\mathbf{t})$  exerted by the particle of species  $\beta$  at  $\mathbf{r}_2$  and (ii) the force  $\mathbf{f}_{\gamma}^d(\mathbf{t})$  exerted by all the other particles. Thereby, the total mean force  $\mathbf{F}_{\beta\gamma}(\mathbf{t})$  reads

$$\mathbf{F}_{\beta\gamma}(\mathbf{t}) = \mathbf{f}_{\beta\gamma}(\mathbf{t}) + \mathbf{f}_{\gamma}^d(\mathbf{t}), \quad (8)$$

Assuming that the dumbbell and fluid species are spherical particles interacting through central force potentials, the component of  $\mathbf{f}_{\beta\gamma}$  along  $\mathbf{t}$  is given by

$$f_{\beta\gamma}(\tau \equiv |\mathbf{t}|) = -\frac{du_{\beta\gamma}(\tau)}{d\tau}, \quad (9)$$

where  $u_{\beta\gamma}(\tau)$  is the potential of direct interaction between the two dumbbell particles. The elementary force  $d\mathbf{f}_{\gamma}^d$  produced by a fluid element at  $\mathbf{r}_3$  is given by  $d\mathbf{f}_{\gamma}^d = \sum_{i=1}^k \mathbf{f}_{\gamma i}(\mathbf{r}_{23}) \rho_i(\mathbf{r}_3) dv_3$ , where  $\mathbf{f}_{\gamma i}(\mathbf{r}_{23})$  is the force between a particle of species  $i$  [of local density  $\rho_i(\mathbf{r}_3) \equiv \rho_i g_{\beta\gamma i}^{[3]}(\mathbf{r}_3; \tau)$ ] at  $\mathbf{r}_3$  and the dumbbell's test particle of species  $\gamma$ . The component of  $d\mathbf{f}_{\gamma}^d$  along the direction of  $\mathbf{t}$  is given by

$$df_{\gamma}^d = \sum_{i=1}^k \hat{\mathbf{t}} \cdot \mathbf{f}_{\gamma i}(\mathbf{r}_{23}) \rho_i(\mathbf{r}_3) dv_3 = -\sum_{i=1}^k \hat{\mathbf{t}} \cdot \hat{\mathbf{r}}_{23} \frac{du_{\gamma i}(\mathbf{r}_{23})}{dr_{23}} \rho_i(\mathbf{r}_3) dv_3, \quad (10)$$

with  $\hat{\mathbf{t}}$  and  $\hat{\mathbf{r}}_{23}$  being unit vectors along the  $\mathbf{t}$  and  $\mathbf{r}_{23}$  directions, respectively,  $u_{\gamma i}(\mathbf{r}_{23})$  is the potential of interaction between an  $i$ -species particle with the  $\gamma$ -species particle. Substituting

Eqs. (9) and (10) into Eq.(8),  $F_{\beta\gamma}$  is given by [33, 37]

$$F_{\beta\gamma}(\tau) = -\frac{dw_{\beta\gamma}(\tau)}{d\tau} = -\frac{du_{\beta\gamma}(\tau)}{d\tau} - \sum_{i=1}^k \rho_i \int \frac{du_{\gamma i}(\mathbf{r}_{23})}{dr_{23}} \cos \Omega g_{\beta\gamma i}^{[3]}(\mathbf{r}_3; \tau) dv_3, \quad (11)$$

where  $\hat{\mathbf{t}} \cdot \hat{\mathbf{r}}_{23} = \cos \Omega$  and  $w_{\beta\gamma}(\tau)$  is the potential of mean force between the two dumbbell's particles. According to Eq. (1),

$$w_{\beta\gamma}(\tau) = -k_B T \ln [g_{\beta\gamma}(\tau)], \quad (12)$$

and thus

$$k_B T \frac{d \ln g_{\beta\gamma}(\tau)}{d\tau} = -\frac{du_{\beta\gamma}(\tau)}{d\tau} - \sum_{i=1}^k \rho_i \int \frac{du_{\gamma i}(\mathbf{r}_{23})}{dr_{23}} \cos \Omega g_{\beta\gamma i}^{[3]}(\mathbf{r}_3; \tau) dv_3, \quad (13)$$

which is the Born-Green-Yvon (BGY) equation. The degree of accuracy of  $g_{\beta\gamma}(\tau)$  depends on the method used to compute  $g_{\beta\gamma i}^{[3]}(\mathbf{r}_3; \tau)$ . If  $g_{\beta\gamma i}^{[3]}(\mathbf{r}_3; \tau)$  is computed through the TPE of integral equation theories, it was shown that new diagrams are included in the cluster expansion of  $g_{\beta\gamma}^{(2)}(\tau)$  [37] (see Fig. 3). By examination of the transformation of the Mayer diagrams through the formalism outlined above, the denomination of *three point extension* becomes clear. A more detailed description of TPE can be found in ref. [37].

### C. Application to the RPM electrolyte

In the RPM electrolyte the fluid is considered as made up of hard spheres of diameter  $a$  with a central charge  $q_i = z_i e$ , where  $z_i$  is the valence of species  $i$  and  $e$  is the protonic charge. The electroneutrality condition for the  $n$ -component electrolyte is

$$\sum_{i=1}^n z_i \rho_i = 0. \quad (14)$$

Assuming that the dumbbell particle ( $\alpha$  species) is made up of two particles of the same species from that in the fluid (see Fig. 2), the TPE-HNC/MSA equations become

$$g_{\alpha i}(\mathbf{r}_3) = \exp \left\{ -\beta u_{\alpha i}(\mathbf{r}_3) + \sum_{m=1}^k \rho_m \int h_{\alpha m}(\mathbf{r}_4) c_{mi}(\mathbf{r}_{34}) d\mathbf{r}_4 \right\}, \quad (15)$$

where

$$u_{\alpha i}(\mathbf{r}_3) = u_{\alpha i}(r_{13}, r_{23})$$

$$= \begin{cases} \frac{z_i z_\beta e^2}{\varepsilon r_{23}} + \frac{z_i z_\gamma e^2}{\varepsilon r_{13}} & \text{if } r_{13} \text{ and } r_{23} > a \\ \infty & \text{if } r_{13} \text{ or } r_{23} \leq a \end{cases} \quad (16)$$

with  $z_\beta$  and  $z_\gamma$  standing for valence number of particles  $\beta$  and  $\gamma$ , respectively. For spherical ions the direct correlation function depends only of the ions distance  $r_{34} = |\mathbf{r}_{34}|$ . Within the mean spherical approximation, its analytical expression is

$$c_{mi}(r_{34}) = c^{hs}(r_{34}) + z_m z_i c^{sr}(r_{34}) - \beta \frac{z_m z_i e^2}{\varepsilon r_{34}}, \quad (17)$$

where  $c^{hs}(r_{34})$  is the direct correlation function for a hard spheres fluid in the PY approximation and  $c^{sr}(r_{34})$  is a short ranged function. Because of the symmetry around the dumbbell axis, it is convenient to use prolate coordinates  $(\eta, \xi, \phi)$  [36, 71] defined as follows

$$\begin{aligned} x &= \frac{\tau}{2} \sqrt{(\eta^2 - 1)(1 - \xi^2)} \cos \phi, \\ y &= \frac{\tau}{2} \sqrt{(\eta^2 - 1)(1 - \xi^2)} \sin \phi, \\ z &= \frac{\tau}{2} \eta \xi, \end{aligned} \quad (18)$$

and where the volume element is given by

$$dv = \frac{\tau^3}{8} (\eta^2 - \xi^2) d\phi d\xi d\eta. \quad (19)$$

The relative distance  $r_{34}$  is then given by

$$\begin{aligned} r_{34}^2 &= \frac{\tau^2}{4} \left\{ (\eta_3^2 - 1)(1 - \xi_3^2) + (\eta_4^2 - 1)(1 - \xi_4^2) + (\eta_3 \xi_3 - \eta_4 \xi_4)^2 \right. \\ &\quad \left. - 2\sqrt{(\eta_3^2 - 1)(1 - \xi_3^2)(\eta_4^2 - 1)(1 - \xi_4^2)} \cos \phi_4 \right\}. \end{aligned} \quad (20)$$

In prolate coordinates the potential of electrostatic interaction,  $u_{\alpha i}^{\text{el}}$ , between the dumbbell and one fluid ion of species  $i$  can be conveniently rewritten as

$$u_{\alpha i}^{\text{el}}(\eta, \xi) = \frac{2e^2}{\tau\varepsilon} \left( \frac{z_\beta}{\eta - \xi} + \frac{z_\gamma}{\eta + \xi} \right), \quad (21)$$

and Eq. (15) as



$$\begin{aligned}
g_{\alpha i}(\eta_3, \xi_3) &= g_{\beta\gamma i}^{[3]}(\eta_3, \xi_3; \tau) = \exp \left\{ -\frac{2\beta e^2}{\tau\varepsilon} \left( \frac{z_\beta}{\eta_3 - \xi_3} + \frac{z_\gamma}{\eta_3 + \xi_3} \right) \right. \\
&+ \int_{-1}^1 \int_{\eta_0(\xi_4)}^\infty \rho_{\alpha s}(\eta_4, \xi_4) K(\eta_3, \xi_3, \eta_4, \xi_3) d\eta_4 d\xi_4 \\
&+ z_i \int_{-1}^1 \int_{\eta_0(\xi_4)}^\infty \rho_{\alpha d}(\eta_4, \xi_4) L(\eta_3, \xi_3, \eta_4, \xi_4) d\eta_4 d\xi_4 \\
&\left. - z_i \int_{-1}^1 \int_{\eta_0(\xi_4)}^\infty \rho_{\alpha d}(\eta_4, \xi_4) A(\eta_3, \xi_3, \eta_4, \xi_4) d\eta_4 d\xi_4 - J(\eta_3, \xi_3) \right\}, \quad (22)
\end{aligned}$$

with

$$\eta_0(\xi) = \begin{cases} \xi + b & \text{for } \xi_0 < \xi \leq 1 \\ 1 & \text{for } 0 \leq \xi \leq \xi_0 \end{cases}$$

and  $\xi_0 = 1 - b$ ,  $b \equiv 2a/\tau$  and  $\eta_0(-\xi) = \eta_0(\xi)$ . The expressions for  $K$ ,  $L$ ,  $A$ ,  $J$ ,  $\rho_{\alpha s}$  and  $\rho_{\alpha d}$  are

$$K(\eta_3, \xi_3, \eta_4, \xi_4) = \frac{\tau^3}{8}(\eta_4^2 - \xi_4^2) \int_0^{\phi_{\max}} c^{\text{hs}}(r_{34}) d\phi_4,$$

$$L(\eta_3, \xi_3, \eta_4, \xi_4) = \frac{\tau^3}{8}(\eta_4^2 - \xi_4^2) \int_0^{\phi_{\max}} c^{\text{sr}}(r_{34}) d\phi_4,$$

$$A(\eta_3, \xi_3, \eta_4, \xi_4) = -\frac{\tau^4 \beta e^2}{8\varepsilon}(\eta_4^2 - \xi_4^2) \int_0^{2\pi} \frac{d\phi_4}{r_{34}},$$

$$\rho_{\alpha s}(\eta_4, \xi_4) = \rho_{\beta\gamma s}(\eta_4, \xi_4) \equiv \sum_{m=1}^n \rho_m h_{\alpha m}(\eta_4, \xi_4),$$

$$\rho_{\alpha d}(\eta_4, \xi_4) = \rho_{\beta\gamma d}(\eta_4, \xi_4) \equiv \sum_{m=1}^n z_m \rho_m h_{\alpha m}(\eta_4, \xi_4),$$

$$J(\eta_3, \xi_3) = \int_{-1}^{-\xi_{\min}(\tau)} \int_1^{\eta_0(\xi_4)} K(\eta_4, \xi_4, \eta_3, \xi_3) d\eta_4 d\xi_4 + \int_{\xi_{\min}(\tau)}^1 \int_1^{\eta_0(\xi_4)} K(\eta_4, \xi_4, \eta_3, \xi_3) d\eta_4 d\xi_4,$$

respectively, with

$$\xi_{\min}(\tau) = \begin{cases} 0 & \text{if } \tau \leq a \\ \xi_0 & \text{if } \tau > a. \end{cases}$$

By introducing the elliptic function of second kind  $F(\pi/2, k)$ , one can rewrite  $A$  as

$$A(\eta_3, \xi_3, \eta_4, \xi_4) = \frac{\tau(\eta_3^2 - \xi_3^2) F(\pi/2, k)}{2r_{34}^{\text{max}}} \quad (23)$$

where

$$k^2 = \frac{\tau^2 \sqrt{(\eta_3^2 - 1)(1 - \xi_3^2)(\eta_4^2 - 1)(1 - \xi_4^2)}}{2(r_{34}^{\text{max}})^2}, \quad (24)$$

and

$$(r_{34}^{max})^2 = \frac{\tau^2}{4} \left[ \sqrt{(\eta_3^2 - 1)(1 - \xi_3^2)} + \sqrt{(\eta_4^2 - 1)(1 - \xi_4^2)} \right]^2 + (\eta_3 \xi_3 - \eta_4 \xi_4)^2. \quad (25)$$

Eq. 22 is in fact a set of two coupled, three dimensional, non-linear integral equations. To solve these equations, we have developed a sophisticated, but efficient, finite element method for its solution (see appendix for details on our numerical method).

Using Eq. (11), the mean force between the two dumbbells particles reads

$$F_{\beta\gamma}(\tau) = f_{\beta\gamma}^*(\tau) + f_{\beta\gamma}^{el}(\tau), \quad (26)$$

where

$$f_{\beta\gamma}^*(\tau) = \frac{\pi\tau^2}{2\beta} \sum_{j=1}^2 \rho_j \int_{\xi_{\min}(\tau)}^1 g_{\beta\gamma j}^{[3]}[\eta_0(\xi_3), \xi_3; \tau] \left[ -2\xi_3^3 - 3b\xi_3^2 + (2 - b^2)\xi_3 + b \right] d\xi_3 \quad (27)$$

and

$$f_{\beta\gamma}^{el}(\tau) = \frac{z_\beta z_{\gamma_3} e^2}{\varepsilon \tau^2} + \frac{\tau \pi z_\beta e^2}{\varepsilon} \int_{-1}^1 \int_{\eta_0(\xi_3)}^\infty \rho_{\beta\gamma d}(\eta_3, \xi_3) \frac{(1 - \eta_3 \xi_3)(\eta_3 + \xi_3)}{(\eta_3 - \xi_3)^2} d\xi_3 d\eta_3. \quad (28)$$

Thus the pair distribution function of the electrolyte solution is given by

$$g_{\beta\gamma}(r) = \exp \left\{ -\beta \int_\infty^r F_{\beta\gamma}(\tau) d\tau \right\}. \quad (29)$$

The solution of Eq. (22) and calculation of  $F_{\beta\gamma}$  through Eqs. (26), (27) and (28) were numerically solved.

### III. MOLECULAR DYNAMICS

The electrolyte is confined in a cubic box of length  $L$ . The bulk salt concentration  $\rho$  is then given by  $\frac{N}{L^3}$ , where  $N$  is the number of positive (or negative) ions. The dumbbell is made up of two *fixed* ions (with a center-center separation  $\tau$ ) disposed symmetrically along the axis passing by the two centers of opposite faces. A similar system setup was also used elsewhere to study two fixed macroions [72, 73, 74]. We use MD simulations to compute the motion of the mobile fluid ions coupled to a heat bath acting through a weak stochastic force  $\mathbf{W}_i(t)$  with a zero mean value. The equation of motion of any mobile ion  $i$  reads

$$m \frac{d^2 \mathbf{r}_i}{dt^2} = -\nabla_i U - m\Gamma \frac{d\mathbf{r}_i}{dt} + \mathbf{W}_i(t), \quad (30)$$

where  $m$  is the ion mass,  $\Gamma$  is the friction coefficient and  $-\nabla_i U$  is the potential force having two contributions: (i) the Coulomb interaction and (ii) the excluded volume interaction. Friction and stochastic force are linked by the dissipation-fluctuation theorem  $\langle \mathbf{W}_i(t) \cdot \mathbf{W}_j(t') \rangle = 6m\Gamma k_B T \delta_{ij} \delta(t - t')$ .

Excluded volume interactions are modeled by a pure repulsive Leonard-Jones ( $LJ$ ) potential defined by

$$U_{LJ}(r) = \begin{cases} 4\epsilon_{LJ} \left[ \left(\frac{a}{r}\right)^{12} - \left(\frac{a}{r}\right)^6 \right] + \epsilon_{LJ}, & \text{for } r < 2^{1/6}a \\ 0, & \text{for } r \geq 2^{1/6}a, \end{cases} \quad (31)$$

where  $a$  is the ion diameter.

The electrostatic interaction between any pair  $ij$ , where  $i$  and  $j$  denote either a dumbbell ion and/or a mobile fluid ion, reads

$$U_{el}(r) = \pm k_B T \ell_B \frac{z^2}{r}, \quad (32)$$

where  $+(-)$  applies to ions likely (oppositely) charged,  $\ell_B = \frac{e^2}{\epsilon k_B T}$  is the Bjerrum length describing the electrostatic strength and  $z$  is the salt valence ( $z_i = z_j = z$ ). To link our system parameters to experimental units we choose the  $LJ$  energy parameter  $\epsilon_{LJ} = k_B T$  (where  $T = 298\text{K}$ ) and  $a = 4.25 \text{ \AA}$ . This leads then to the water Bjerrum length  $\ell_B = 1.68a = 7.14 \text{ \AA}$ . A macroscopic system was mimicked by imposing periodic boundary conditions. The long range Coulomb interaction was treated by using an optimized and efficient Ewald summation variant, namely the particle-particle-particle-mesh (P3M) method [75].

In order to limit the size effects, we choose  $L$  sufficiently large, typically 10 times (or more) the Debye-Hückel screening length. The number of ions in the box is 500 for all cases (concentrated and dilute solutions). It is important to mention that the computation of  $g_{\beta\gamma i}^{[3]}(r, \theta; \tau)$  is statistically extremely demanding and especially for small  $\theta$  angles, since the quantity of information varies like  $\sin(\theta)$ . In this notation, the distance  $r \equiv |\mathbf{r}_3|$  and the angle  $\theta \equiv \angle(\mathbf{r}_1, \mathbf{r}_3)$  are always relative to the center of the dumbbell (see Fig. 2). The fact that the observable  $g_{\beta\gamma i}^{[3]}(r, \theta; \tau)$  concerns only an “elementary solid angle”, it strongly reduces the available information compared to that available for the *pair* correlation function, since

in that latter case a full solid angle  $4\pi$  and many ion pairs are accessible. To overcome this difficulty, we considered a sufficiently large angle range  $\Delta\theta$  (typically between  $5 - 15^\circ$  depending on the concentration  $\rho$ ), so that the gathered informations contains as less noise as possible. On the other hand,  $\Delta\theta$  must not to be too large otherwise the resolution gets too small. For each system under consideration, a compromise between these two effects that had to be found.

Finally for the computation of the effective mean force between two ions, we considered the same system but where no fixed dumbbell is present. Thereby, we could compute the potential of mean force, knowing the  $g(r)$ , and then get by derivation the effective force.

#### IV. RESULTS

We have done calculations for the 1:1 and 2:2 electrolytes using the TPE-HNC/MSA integral equation. *For the 1:1 electrolyte the agreement between TPE-HNC/MSA and MD results is qualitative and quantitatively very good.* However, in order to keep low the number of plots we just present a detailed analysis on the results of the 2:2 electrolyte. The choice of divalent ions is motivated by the fact that it represent a strong test for liquid theories. Thereby, we considered two typical concentrations: (i) the concentrated case with  $\rho = 1\text{M}$  and (ii) the dilute case with  $\rho = 0.005\text{M}$ . As a main result, the effective mean force obtained by TPE-HNC/MSA, HNC/MSA, and MD simulation is presented for each concentration regime. In order to further quantify the robustness of the TPE-HNC/MSA theory, we investigated in detail the conditional three-particle distribution function,  $g_{\beta\gamma i}^{[3]}(r, \theta; \tau)$ , by comparing TPE-HNC/MSA with MD.

For the discussion, it is convenient to adopt the following notations:  $g_{++-}^{[3]}(r, \theta; \tau)$  stands for the distribution function of negative ions when the dumbbell is made up of two positive ions,  $g_{+--}^{[3]}(r, \theta; \tau)$  for that of negative ions when the dumbbell is made up of a negative and a positive ions, and so on. By symmetry the three particle distribution function satisfies  $g_{++-}^{[3]}(r, \theta; \tau) = g_{--+}^{[3]}(r, \theta; \tau)$  and also  $g_{+--}^{[3]}(r, \theta; \tau) = g_{+-+}^{[3]}(r, \pi - \theta; \tau)$ . Thereby, we systematically compared theory and simulation for  $g_{\beta\gamma i}^{[3]}(r, \theta; \tau)$ , but show results only for  $g_{\beta\gamma i}^{[3]}(r, \theta; \tau = a)$  (i.e., when the two dumbbell ions are in contact), for two given values of  $\theta$  ( $\pi/4$  and  $\pi/2$ ). In addition, within the TPE-HNC/MSA theory, we also provide the full  $\theta$ -dependence of  $g_{\beta\gamma i}^{[3]}(r, \theta; \tau)$  for different  $\tau$ .

## A. Concentrated case

In this section, we deal with the concentrated electrolyte solution ( $\rho = 1 \text{ M}$ ). The electrostatic screening at such high ionic density and valence ( $z = 2$ ) is very strong. The study of such a system is important to test TPE-HNC/MSA theory, since already inhomogeneous and homogeneous HNC/MSA theories are in excellent agreement with molecular simulations under such conditions [76].

### 1. Three particle correlation function

*a. Symmetric dumbbell* We first consider symmetric dumbbells made of like charged positive divalent ions. The profiles of  $g_{++-}^{[3]}(r, \theta = \pi/2; \tau = a)$  and  $g_{+++}^{[3]}(r, \theta = \pi/2; \tau = a)$  are depicted in Fig. 4. Concerning the negatively charged fluid ions (i.e., “dumbbell counter-ions”), we have quantitative agreement between theory and simulation even near the distance of closest approach. The slight difference at short distance ( $r \sim a$ ) is due to the fact that for the short-ranged excluded volume interaction, MD simulation is built with a soft-core  $LJ$  potential whereas the actual theory uses a true hard-core potential. For the positively charged fluid species (“dumbbell co-ions”), we also have an excellent qualitative agreement. The TPE-HNC/MSA maximum of the co-ion distribution function is within the statistical error, however slightly higher than MD data. The location of the maximum is nearly the same as that found with simulation. Hence TPE-HNC/MSA has an excellent agreement with MD, within the numerical error.

For  $\theta = \pi/4$  (see Fig. 5), one still has the same quantitative agreement between MD and TPE-HNC/MSA for the dumbbell counter-ions. It is observed that the value of  $g_{++-}^{[3]}(r, \pi/4; a)$  at closest approach ( $r = 1.29a$ ) is not as high as at  $\theta = \pi/2$  (see Fig. 4) for the corresponding plot. The physical reason of this feature is straightforward. The closest approach to the center of the dumbbell is larger at  $\theta = \pi/4$  than at  $\theta = \pi/2$ , therefore, since all particles have the same size, the resulting *attractive* electrostatic interaction between the dumbbell and the counter-ion is higher at  $\theta = \pi/2$ . For the dumbbell-co-ions distribution  $g_{+++}^{[3]}(r, \pi/4; a)$  we have quantitative agreement between TPE-HNC/MSA and MD.

The three dimensional (3D) plots of the three particle (counter-ion-dumbbell) distribution function  $g_{++-}^{[3]}(r, \theta; \tau)$  obtained by TPE-HNC/MSA are sketched in Fig. 6. At  $\tau = a$

(dumbbell ions at contact), Fig. 6(a) shows a strong variation near to the surface of closest approach. As expected, the maximum is obtained at  $\theta = \pi/2, 3\pi/2$  ( $g_{++-}^{[3]} \approx 50$ ), whereas the minimum is at  $\theta = 0, \pi$  ( $g_{++-}^{[3]} \approx 8$ ). Moreover, we have oscillations in the distribution function, as a function of  $r$ , for any  $\theta$ , which confirms our previous observations at  $\theta = \pi/2, \pi/4$  (see Figs. 4 and 5). We have carefully checked that this feature holds at any  $\tau$ . The 3D plot of the co-ion-dumbbell distribution  $g_{+++}^{[3]}(r, \theta; a)$  is not reported here.

At a larger dumbbell separation,  $\tau = 2a$  [see Fig. 6 (b)],  $g_{+++}^{[3]}(r, \theta; 2a)$  is still highly peaked at  $\theta = \pi/2$  and has its maximal value at the middle point of the dumbbell. At sufficiently large separation, we have an isotropic counter-ion distribution around each dumbbell particle (not shown here). We point out that although the probability of finding two like-charged ions in contact ( $\tau = a$ ) is very low, the probability of having more than two counter-ions in contact (at  $\theta \approx \pi/2$ ) with the two like-charged ions dumbbell, is very high. This implies an overcompensation of the dumbbell's charge, which is verified by the observed oscillations in the counter-ions profile of Fig.6, since oscillations imply an electrical field inversion, which implies charge reversal. It should be stressed that to calculate thermodynamics functions such as the internal energy or pressure,  $g_{++i}^{[3]}(r, \theta; \tau)$  for every  $\tau$  must be known, even if the probability of finding two like-charged ions at contact is very low.

*b. Antisymmetric dumbbell* We now consider antisymmetric dumbbells made of two opposite divalent ions. In this case, by symmetry arguments we expect that  $g_{+--}^{[3]}(r, \pi/2; a) = g_{+-+}^{[3]}(r, \pi/2; a)$ . The profiles of  $g_{+--}^{[3]}(r, \pi/2; a)$  and  $g_{+-+}^{[3]}(r, \pi/2; a)$  are plotted in Fig. 7. Since at  $\theta = \pi/2$  the electric field component (produced by the dumbbell) perpendicular to the dumbbell axis is zero, the electrostatic correlations are only generated by the fluid ions. Consequently, we expect a quasi-neutral fluid behavior. This is precisely what Fig. 7 shows for theory and simulation, where  $g_{+--}^{[3]}(r, \pi/2; a)$  and  $g_{+-+}^{[3]}(r, \pi/2; a)$  curves collapse in a single curve. The adsorption at contact, is a hard sphere entropic effect due to the salt high concentration. This adsorption does not occur at low salt concentration.

Results for  $\theta = \pi/4$  are shown in Fig. 8. We have again a very satisfactory agreement between theory and simulation.

The 3D plot of  $g_{+--}^{[3]}(r, \theta; \tau = a) = g_{+-+}^{[3]}(r, \pi - \theta; \tau = a)$  obtained by TPE-HNC/MSA is sketched in Fig. 9. The maximum and minimum are located at  $\theta = 0$  and  $\theta = \pi$  at dumbbell contact, which implies a high probability of a line quadruplet configuration. However, if we look at Fig.7, it implies that, although with a lower probability, positive or

negative ions are adsorbed around the center of the antisymmetric dumbbell, at  $\theta = \pi/2$ . Again, we observe oscillations at any  $\theta$  angle, and we checked that it is the case for any  $\tau$ . Hence, charge reversal is also present, implying that more than two ions are adsorbed to the dumbbell. Thus, probably compact clusters more than line clusters are formed at this high concentration. We will come back to this point later.

## 2. Effective force

The effective mean force between two like charges [ $F_{++}(r)$ ] and that between two opposite charges [ $F_{+-}(r)$ ] as a function of their mutual separation  $r$  are depicted in Fig. 10, in reduced units of  $\frac{k_B T}{\ell_B}$ . As expected, theories (TPE-HNC/MSA and HNC/MSA) and simulation are in very good agreement for both forces  $F_{++}(r)$  and  $F_{+-}(r)$ .

An interesting feature is the kink in  $F_{++}(r)$  occurring at  $r = 2a$ , that is somewhat less marked, however present, on the simulation plot (due to the softness of the ions and also the lower radial resolution there). This jump in the first derivative,  $F'_{++}(r)$ , at  $r = 2a$  is not an artifact of the theory (or the simulation) but a true physical feature. This effect is due to excluded volume correlations and, in much lesser degree, to electrostatic correlations. It is clear that, at  $r = 2a$ , the configuration consisting of a counter-ion lying exactly between two co-ions (i.e.,  $+ - +$ ) is energetically very favorable (see Fig. 6b). This implies the formation of ion complexes, in qualitative agreement with Caillol and Weiss [17] and Yan and de Pablo [21]. When  $r > 2a$  (more precisely  $r \rightarrow 2a^+$ ), the presence of an in-between counter-ion leads to a relatively strong resistance, on the level of the depletion force, upon approaching the two co-ions. On the other hand, when  $r < 2a$  (more precisely  $r \rightarrow 2a^-$ ), the absence of an in-between counterion leads to an easier approach (on the level of the depletion force) of the two co-ions. These mechanisms, explain (i) the discontinuity of  $F'_{++}(r)$  at  $2a$  and (ii) the fact that  $|F'_{++}(r \rightarrow 2a^-)| < |F'_{++}(r \rightarrow 2a^+)|$ . This effect should also be observed in *neutral* hard spheres systems at sufficiently high density, and in the interaction between two macroions.

As far as the force  $F_{+-}(r)$  is concerned, this kind of discontinuity in the derivative is absent or nearly undetectable. This is due to the fact that, at  $r = 2a$ , the probability of finding the configuration consisting of an ion between two oppositely ions (i.e.,  $+ - -$ ) is considerably smaller compared to that obtained with the configuration  $+ - +$ .  $F_{+-}(r) < 0$

and  $F_{++}(r) > 0$  are of the same order of magnitude and indicate, of course, that the  $(+-)$  configuration is of high probability, whereas the  $(++)$  is of low probability.

By definition  $\ln g_{\beta\gamma i}^{[3]}(r, \theta; \tau) \equiv -w_{\beta\gamma i}(r, \theta, \tau)/k_B T$ . Hence,  $\rho_i g_{\beta\gamma i}^{[3]}(r, \theta; \tau)$  gives the probability of finding an ion of species  $i$ , at a certain position  $(r, \theta)$ , from a dumbbell made of two ions of species  $\beta$  and  $\gamma$ , located at a distance  $\tau$ , from each other.  $w_{\beta\gamma i}(r, \theta, \tau)$  is the potential of mean force between the ion  $i$  and the dumbbell. The mean internal energy of an ideal gas per particle is  $3k_B T/2$ . Hence,  $-W_0 \equiv -w_{++-}(r, \theta, \tau)/[k_B T] > 3/2$ , for a plus-plus pair, i.e.  $g_{++-}^{[3]}(r, \theta; \tau) > 4.48$ , implies that a counter-ion next to a like-charged dumbbell has an adsorption energy larger than its thermal energy, and thus it is tightly attached to the dumbbell. For a 1M electrolyte,  $-W_0 > 3/2$  implies  $\rho_- g_{++-}^{[3]}(r, \theta; \tau) > 4.48 M$ . In Fig. 6a, the peak is for  $\rho_- g_{++-}^{[3]}(r_0, \theta = \pi/2; \tau = a) = 50M \gg 4.48M$ , i.e.,  $-w_{++-}(r, \theta = \pi/2, \tau = a)/k_B T = 3.9 > 1.5$ . On the other hand, at  $\theta = \pi$ ,  $\rho_- g_{++-}^{[3]}(r_0, \theta = \pi; \tau = a) = 5M$ , i.e.,  $-w_{++-}(r, \theta = \pi, \tau = a)/k_B T = 1.6 \simeq 1.5$ . Therefore, a negative ion will be strongly attached to the positive ions pair (at  $\theta = \pi/2$ ). A simple calculation shows that the unscreened attractive electrostatic energy of a second negative ion to the  $(++-)$  ion complex decreases to around 50% of the attractive energy of the positive ion pair to the first negative ion. Hence, a second adsorbed ion, at  $\theta = \pi/2$ , seems likely. Thus, Fig. 6a suggest a quadruplet structure, where the two counter-ions are at  $\theta = \pi/2$ . Clearly, more than two counter-ions are adsorbed, since the dumbbell charge is overcompensated, i.e., there are concentration profile oscillations. The adsorption of these additional counter-ions is due to the short range correlations, i.e., ions next to the dumbbell feel a net force toward it due to the uneven collisions from bulk ions, and is an entropic effect, beyond the ideal gas entropy. This effect is larger, the larger the electrolyte concentration, and it will *not* be present in a point ion electrolyte. Because the attractive potential of mean force is very high, this compact ion complex structure is very stable, although very unlikely, because  $F_{++}(r) > 0$  (see Fig. 10). However, for  $2a < \tau < 3a$ , a  $(+-+)$  configuration is very likely. Hence, this indicates that there are several mechanisms for the formation of ion complexes.

For the plus-minus pair, in Fig 9 the peak is for  $\rho_+ g_{+--}^{[3]}(r_0, \theta = 0; \tau = a) = 6.8M > 4.48M$ , i.e.,  $-w_{+--}(r, \theta = 0, \tau = a)/k_B T = 1.9 > 1.5$ . and from Fig. 7,  $-w_{+--}(r, \theta = \pi/2, \tau = a)/k_B T = 0.18 \ll 1.5$ . Hence, for an unlike charged dumbbell, we expect an aligned stable quadruplet configuration (because of symmetry), due to energy arguments. However, due to entropic effects more counter-ions are adsorbed into the dumbbell, producing charge



reversal, as can be seen from the oscillations of Fig.9. These additional ions are delocalized around the dumbbell, hence, generating compact ion complexes because  $F_{+-}(r) < 0$  (see Fig. 10), this configuration is very likely.

## B. Dilute case

In this section, we study a dilute, divalent electrolyte ( $\rho = 0.005\text{M}$  and  $z = 2$ ). To the best of our knowledge *all of the known liquid theories fail to describe the RPM behavior under these conditions* [7, 11]. Hence, the study of low concentrated solutions of multivalent ions represents a strong test case for a liquid theory. In addition, for the RPM electrolyte we are on the low concentration side of the phase diagram.

### 1. Three particle correlation function

*a. Symmetric dumbbell* Figures 11(a) and 11(b) show a comparison between TPE-HNC/MSA and MD results for  $g_{++-}^{[3]}(r, \pi/2; a)$  and  $g_{+++}^{[3]}(r, \pi/2; a)$ , respectively. One can see that the electrical double layer is wider than in the concentrated case i.e., the correlations are long ranged. For  $g_{++-}^{[3]}(r, \pi/2; a)$  [see Fig. 11(a)], TPE-HNC/MSA and MD results show quantitative agreement, even near contact. For the  $g_{+++}^{[3]}(r, \theta = \pi/2; a)$  [see Fig. 11(b)], a qualitative agreement between TPE-HNC/MSA and MD results is found.

At  $\theta = \pi/4$  (see Fig. 12) it is found that the contact value of  $g_{++-}^{[3]}(r, \pi/4; a)$  (about 500) is much smaller, of two orders of magnitude, than that at  $\theta = \pi/2$ . This can be explained in terms of the electric field produced by the dumbbell at  $\theta = \pi/2$  which is considerably stronger than at  $\theta = \pi/4$ .

The 3D plot of  $\ln(g_{++-}^{[3]}(r, \theta; \tau))$  can be found in Fig. 13. For  $\tau = a$  [see Fig.13 (a)], it is observed a strong variation of the distribution function close to the dumbbell (at the surface of closest approach). As expected, the maximum of  $g_{++-}^{[3]}(r, \theta; a)$  is at  $\theta = \pi/2$ . On the other hand, at  $\tau = 5a$  (see Fig. 13(b)), the angular variation of  $g_{++-}^{[3]}(r, \theta; 5a)$  (near contact) around one ion of the dumbbell is not as peaked as in  $g_{++-}^{[3]}(r, \theta; a)$ . However, the dumbbell ions are still correlated, i.e., their electrical double layers are strongly *overlapped* although  $\tau = 5a$ . We had to go up to  $\tau = 60a$  (not shown) to cancel the overlapping of the electrical double layers of the dumbbell ions. At low salt concentration there is a longer

range penetration of the ions electrical field into the fluid, and hence charge correlations are of longer range. For low salt concentration the role of higher order diagrams is more important. It is observed that *for this low concentration case, there are no oscillations* in the counterion concentration profiles. Hence, no charge reversal is present and, thus, the formation of a simple more complex ionic configurations, beyond a quadruplet formation, is not supported by our results. Because of the very large value of  $W_0 \approx 8.6$ , the adsorption of two counter-ions to the like-charged dumbbell (at  $\theta = \pi/2$ ) is much larger than for the equivalent situation for the concentrated case, where  $W_0 \approx 3.9$ . Hence, for the dilute case the quadruplet is more stable, but even less probable due to the lower concentration.

*b. Antisymmetric dumbbell* We now consider the three particle distribution function where the dumbbell is made up of two opposite ions, and for the same fluid parameters as in Figs. 11 and 12. Only the case of  $\theta = \pi/4$  is shown (see Fig. 14), given that for  $\theta = \pi/2$  the electrical field is zero and since the electrolyte concentration is very low we have  $g_{+--}^{[3]}(r, \theta = \pi/2) = g_{+--+}^{[3]}(r, \theta = \pi/2) \approx 1$ . This is in contrast with the 1M electrolyte result of Fig. 7. For  $\theta = \pi/2$  the same good agreement is found between TPE-HNC/MSA and MD as that in Fig. 12.

The 3D plot of  $\ln g_{+--}^{[3]}(r, \theta; \tau = a) = \ln g_{+--+}^{[3]}(r, \pi - \theta; \tau = a)$  which is the potential of mean force is sketched in Fig. 15. This function is quasi center-symmetric with respect to the dumbbell center. This feature is due to (i) the symmetry of the electrostatic correlations and (ii) the fact that the contribution of the excluded volume correlations (at such low density) is negligible compared to that in the concentrated case. As expected the function is strongly peaked at  $\theta = 0$ . For the concentrated case (not shown) the asymmetry is higher. The important result shown in this figure is the formation of a stronger (+ - + -) line quadruplet, than for the concentrated case, since here  $-w_{+--}(r = 3/2a, \theta = 0, \tau = a)/k_B T = -w_{+--+}(r = 3/2a, \theta = \pi, \tau = a)/k_B T \approx 4.2 > 1.5$ , which is much higher than that for the corresponding concentrated case ( $-w_{+--}(r = 3/2a, \theta = 0, \tau = a)/k_B T \approx 1.6$ ). Hence, this line quadruplet structure would be more stable. This result suggests that quadruplets, if present, would be in a linear configuration more than in compact quadruplets structures, in disagreement with Fig. 4 of Yan and de Pablo [21, 77].

## 2. Effective force

The effective mean force between two like charges [ $F_{++}(r)$ ] and that between two opposite charges [ $F_{+-}(r)$ ] as a function of their mutual separation  $r$  can be found in Fig. 16, in reduced units of  $\frac{k_B T}{\ell_B}$ . Concerning  $F_{+-}(r)$ , theories (TPE-HNC/MSA and HNC/MSA) and simulation are in quantitative agreement.

As pointed out above, for  $F_{++}(r)$  in the concentrated case, the derivative  $F'_{++}(r)$  is again discontinuous at  $r = 2a$ . The same mechanism proposed for the concentrated case (see Sec. IV A 2) applies here. This important feature is not captured by HNC/MSA, proving the qualitative improvement by using the TPE method. This better description stems from proper inclusion of long ranged correlations. Finally, we have a good quantitative agreement between TPE-HNC/MSA and MD. In comparison of Fig. 16, with that for the concentrated case, Fig. 10, two important differences are observed: The intensity and the range of the force is larger for the dilute case, implying that the electrical field is less screened. Also for low concentration  $F_{++} > 0$ , i. e., it is always repulsive, whereas in the concentrated regime, for some interval of  $\tau$ ,  $F_{++}$  is negative, implying an attraction and hence different ion-complexes mechanisms. In addition, one can expect that for a certain combination of temperature, solvent dielectric constant, and salt valence and low concentration, one can find a phase transition, in which associated ions and free ions coexist: *single ions, ion pairs and quadruplets*. Hence, from Figs. 9 and 10, for the concentrated case, and Figs. 15 and 16, for the dilute case, we conclude that linear ion complexes are likely to be formed. At low concentration, dumbbells (+-) and line quadruplets (+ - +-) are very likely to be formed, whereas at high concentration larger complexes than quadruplets are formed. This is in qualitative agreement with the predictions of Caillol and Weiss [17].

## V. CONCLUSIONS

We have investigated the structure of 1:1 and 2:2 RPM electrolytes by means of integral equations and MD simulations. Using the three point extension to the HNC/MSA theory, the conditional three particle distribution function,  $g^{[3]}(r, \theta; \tau)$ , was computed and compared with that obtained by MD. Although it is not shown, for the 1:1 electrolyte the quantitative agreement between TPE-HNC/MSA and MD is excellent. For the 2:2 electrolyte, we explic-

itly report here results for two typical concentrations: (i) the concentrated case ( $\rho = 1\text{M}$ ) and (ii) the dilute case ( $\rho = 0.005\text{M}$ ).

As far as the concentrated case concerns, it was found that  $g^{[3]}(r, \theta)$  always presents oscillations. The detailed comparison between TPE-HNC/MSA and MD, carried at fixed separation  $\tau = a$  (between the two constitutive ions of the dumbbell), shows an excellent qualitative and/or quantitative agreement. This is true for all values of  $\tau$  (not shown).

On the level of the effective mean force between two ions, both, TPE-HNC/MSA and HNC/MSA are in very good agreement with MD. This is consistent with previous comparisons between HNC/MSA and Monte Carlo results [7, 76]. Hence we can conclude that the TPE-HNC/MSA method is also suitable to describe concentrated electrolyte solutions. It is important to point out a particular behavior in the effective force between like-charged ions [ $F_{++}(r)$ ] observed at  $r = 2a$ , where an abrupt change in its slope appears due to excluded volume correlations. This behavior can not be directly seen in the pair distribution function (for this value of  $\rho$ ).

In the dilute regime, the analysis of the three particle distribution function and the effective force shows the long range nature of the correlations. For the three particle distribution functions, we had to go up to a distance separation of  $\tau \approx 60a$ , in order to uncorrelated the two constitutive dumbbell ions. Again a good agreement for  $g^{[3]}(r, \theta)$  is found between TPE-HNC/MSA and MD, proving the robustness of the TPE formalism. The study of the effective force reveals a quantitative agreement for the force between two oppositely charged ions,  $F_{+-}(r)$ , between TPE-HNC/MSA and MD, although HNC/MSA is also very good. For the force  $F_{++}(r)$  we again remark the occurrence of an abrupt change in its slope at  $\tau = 2a$ , which is not predicted by HNC/MSA. On the other hand, TPE-HNC/MSA and MD are in quantitative agreement, showing the ability of TPE to take fairly well into account long range correlations. It is precisely in this region of the ionic fluid phase diagram, i.e., low concentration and high Coulombic coupling, where all the other theories fail.

The TPE approach is a general formalism that improves existing liquid theories, by including higher order diagrams in a systematic, consistent way [37]. Here we have shown it to be successful for ionic fluids, in all the regions of the RPM phase diagram, in particular in the region of low salt concentration and high coulombic coupling.

In the high concentration regime, ion pairs tend to form aligned quadruplets, i.e.,  $(- + - +)$  structures are energetically favored. However, because of short range correlations,

other delocalized ions are adsorbed to produce charge reversal of the unsymmetrical ion dumbbell and hence the formation of larger complexes than quadruplets is favored. In the low concentration regime, the  $(- + - +)$  aligned quadruplet structure is even more stable than for the high concentration case. Hence, dumbbells and aligned quadruplets are likely to be formed. No adsorption of additional ions is present, since there are no oscillations in the concentration profile and, hence, there is no charge reversal of the dumbbell or higher multipoles. In the high concentration regime charge reversal is present, whereas at low concentration there is no charge reversal. Our results clearly indicate the formation of ion pairs and complexes, in agreement with previous theoretical predictions [47, 52, 53, 54, 55, 56, 57, 58] and simulation results [21, 24]. In our theory we *do not* impose ion pairs, and could be useful to explore RPM phase transitions, critical behavior and could provide a means to understand the molecular mechanisms behind fluids phase transitions.

### Acknowledgments

FJA and MLC thank CONACYT (L007E and C086A) and NEGROMEX for their financial support. RM gratefully acknowledges the support of *Labotatoires Européens Associés* (LEA).

## APPENDIX A: NUMERICAL METHOD

### 1. Finite Element Method

To solve the TPE-HNC/MSA equation, Eq. (22), it is necessary to use a numerical method, since an analytical solution is not available. The finite element method (FEM) has been used in the past to solve HNC/MSA equation in several geometries [35, 36, 78] and it has been proved to be efficient. The general form of TPE-HNC/MSA integral equation can be written as

$$g_{\alpha i}(\eta, \xi) = \exp \left\{ M_i(\eta, \xi) + \int_{-1}^1 \int_{\eta_0(\xi)}^{\infty} \sum_{m=1}^2 \rho_m h_{\alpha m}(\eta', \xi') F(\eta, \xi, \eta', \xi') d\eta' d\xi' \right\}, \quad (\text{A1})$$

$$(\text{A2})$$

where  $h_{\alpha m}(\eta, \xi)$  and  $M_i(\eta, \xi)$  are functions defined on a bidimensional domain  $(\eta, \xi) \in [-1, 1] \times [1, \infty)$ . Since  $h_{\alpha m}(\eta, \xi) \neq 0$  only in a region close to the dumbbell, we solve Eq. (A1) just in a finite domain. In the FEM [79], the domain is divided into  $N$  elements. Every element in a domain  $A_K$  is divided into  $L_0$  sub-elements. In prolate coordinates, the dumbbell geometry of Fig. 17 is mapped into the geometry shown in Fig. 18, where one of the  $N$  triangular elements is shown.

In order to solve Eq. (A1), the function  $h_{\alpha m}(\eta, \xi)$  is expanded as a linear combination of a  $L_0$  base elements  $\{\phi_i^K(\eta, \xi), i = 1, \dots, L_0\}$ , where  $1 \leq K \leq N$ . These base functions are defined in such a way that  $\phi_i^K(\eta, \xi) = 0$  if  $(\eta, \xi) \notin A_K$ . Furthermore the base functions are chosen so that for a set of  $L_0$  points  $(\eta_j, \xi_j)$  (which are called nodes, see Fig. 18), they satisfy

$$\phi_i^K(\eta, \xi) = \delta_{ij}, \quad \text{with } i, j = 1, \dots, L_0, \quad (\text{A3})$$

with  $\delta_{ij}$  being the Kronecker delta function. Hence,

$$h_{\alpha m}(\eta, \xi) = \sum_{K=1}^N \sum_{l=1}^{L_0} \omega_{ml}^K \phi_l^K(\eta, \xi), \quad m = 1, 2 \quad (\text{A4})$$

where  $\{\omega_{ml}^K, l = 1, \dots, L_0\}$  are the  $L_0$  coefficients of the  $h_{\alpha m}$  in the  $K$ -th finite element. Thereby, the coefficient  $\omega_{mi}^K$  is the value of the function at the  $i$ -th node, i.e.,

$$\omega_{mi}^K = h_{\alpha m}(\eta_i, \xi_i). \quad (\text{A5})$$

It is useful to renumber  $\phi_l(\eta, \xi)$  and  $\omega_{ml}$ , so that Eq. (A4) can be rewritten as follows

$$h_{\alpha m}(\eta, \xi) = \sum_{l=1}^{M_0} \omega_{ml} \phi_l(\eta, \xi), \quad m = 1, 2 \quad (\text{A6})$$

where

$$\omega_{mi} = h_{\alpha m}(\eta_i, \xi_i) = g_{\alpha m}(\eta_i, \xi_i) - 1, \quad (\text{A7})$$

with  $M_0 = N \times L_0$ , and the superscript  $K$  has been omitted. By substituting Eq. (A6) into Eq. (A1), we get

$$g_{\alpha i}(\eta, \xi) = \exp \left\{ M_i(\eta, \xi) + \sum_{l=1}^{M_0} \sum_{m=1}^2 \rho_m \omega_{ml} C_l(\eta, \xi) \right\}, \quad (\text{A8})$$

where

$$C_l(\eta, \xi) = \int \int_{A_K} \phi_l(\eta', \xi') F(\eta', \xi', \eta, \xi) d\eta' d\xi'. \quad (\text{A9})$$

Evaluating Eq. (A8) at the  $k$ -th node  $(\eta_k, \xi_k)$  and using Eq. (A7), we get

$$\omega_{ik} = \exp \left\{ M_{ik} + \sum_{l=1}^{M_0} \sum_{m=1}^2 \rho_m \omega_{ml} C_{lk} \right\} - 1, \quad (\text{A10})$$

with  $C_{lk} \equiv C_l(\eta_k, \xi_k)$  and  $M_{ik} \equiv M_i(\eta_k, \xi_k)$ . Thus, we have a system of  $2M_0$  non-linear algebraic equations which can be solved by any of the standard methods, for example the Newton's method, which is our method of choice.

## 2. Choice of the base functions $\phi_l(\eta, \xi)$

To construct the base functions, it is necessary to use a coordinate system defined in the element's domain. In our method, we have used the area coordinates  $(L_i)$  defined as follows

$$L_i = \frac{a_i + b_i\eta + c_i\xi}{2\Delta} \quad \text{with } i = 1, 2, 3, \quad (\text{A11})$$

where  $2\Delta$  is the area of the triangular element and

$$\begin{aligned} a_i &= \eta_j \xi_k - \eta_k \xi_j, \\ b_i &= \xi_j - \xi_k, \\ c_i &= \eta_k - \eta_j, \end{aligned} \quad (\text{A12})$$

with cyclic rotation of indexes, where  $j, k = 1, 2, 3$  but  $i \neq j \neq k$ . The set of points  $\{(\xi_i, \eta_i), i = 1, 2, 3\}$  are the coordinates of the triangle corners. The relation between the coordinates  $(\xi, \eta)$  and the triangular coordinates  $\{L_i, i = 1, 2, 3\}$  is given by

$$\begin{aligned} \eta &= L_1\eta_1 + L_2\eta_2 + L_3\eta_3, \\ \xi &= L_1\xi_1 + L_2\xi_2 + L_3\xi_3, \\ 1 &= L_1 + L_2 + L_3. \end{aligned} \quad (\text{A13})$$

The number of nodes is equal to the number of base elements. A quadratic base was used to solve Eq. (A1) and therefore  $L_0 = 6$ . For the corner nodes we have

$$\phi_1 = (2L_1 - 1) L_1, \text{ etc.}, \quad (\text{A14})$$

and for the middle-side nodes

$$\phi_4 = 4L_1L_2, \text{ etc.} \quad (\text{A15})$$

In this coordinate system, Eq.(A9) becomes

$$C_l(\eta, \xi) = 4\Delta \int_0^1 \int_0^{1-L_2} \phi_l(L_1, L_2) \times F(L_1, L_2, \eta, \xi) dL_1 dL_2. \quad (\text{A16})$$

- 
- [1] J. C. Rasaiah and H. L. Fiedman, *J. Chem. Phys.* **50**, 3965 (1969).
  - [2] J. C. Rasaiah, *Chem. Phys. Lett.* **7**, 260 (1970).
  - [3] J. C. Rasaiah, *J. Chem. Phys.* **52**, 704 (1970).
  - [4] J. C. Rasaiah, *J. Chem. Phys.* **56**, 3071 (1972).
  - [5] E. Waisman and J. L. Lebowitz, *J. Chem. Phys.* **56**, 3086 (1972).
  - [6] E. Waisman and J. L. Lebowitz, *J. Chem. Phys.* **56**, 3093 (1972).
  - [7] D. Henderson, M. Lozada-Cassou, and L. Blum, *J. Chem. Phys.* **79**, 3055 (1983).
  - [8] T. L. Croxton and D. A. McQuarrie, *J. Phys. Chem.* **83**, 1840 (1979).
  - [9] D. N. C. J. C. Rasaiah and J. P. Valleu, *J. Chem. Phys.* **56**, 248 (1972).
  - [10] D. N. Card and J. P. Valleeu, *J. Chem. Phys.* **52**, 6232 (1970).
  - [11] S. A. Rogde and B. Hafskjold, *Mol. Phys.* **48**, 1241 (1983).
  - [12] D. A. McQuarrie, *J. Phys. Chem.* **66**, 1508 (1962).
  - [13] L. Belloni, *Phys. Rev. Letts* **57**, 2026 (1986).
  - [14] A. D. Kirschbaum, J. A. Cahil, P. J. McGoingle, and A. V. Grosse, *J. Inorg. Nuclear Chem.* **24**, 1287 (1962).
  - [15] P. N. Vorontsov-Vel'yaminov, A. M. El'yasevich, L. A. Morgenshtern, and V. P. Chasovskikh, *Teplofiz. Vys. Temp.* **8**, 277 (1970).



- [16] P. N. Vorontsov-Vel'yaminov and V. P. Chasovskikh, *Teplofiz. Vys. Temp.* **13**, 1153 (1975).
- [17] J. M. Caillol and J. J. Weis, *J. Chem. Phys.* **102**, 7610 (1995).
- [18] E. Luijten, M. E. Fisher, and A. Z. Panagiotopoulos, *Phys. Rev. Lett* **88**, 185701 (2002).
- [19] A. Z. Panagiotopoulos, *J. Chem. Phys.* **116**, 3007 (2002).
- [20] J. M. Romero-Enrique, G. Orkoulas, A. Z. Panagiotopoulos, and M. E. Fisher, *Phys. Rev. Lett* **85**, 4558 (2000).
- [21] Q. Yan and J. J. de Pablo, *J. Chem. Phys.* **114**, 1727 (2001).
- [22] Q. Yan and J. J. de Pablo, *Phys. Rev. Lett.* **86**, 2054 (2001).
- [23] A. Z. Panagiotopoulos, *Phys. Rev. Lett* **88**, 45701 (2002).
- [24] J. M. Romero-Enrique, L. F. Rull, and A. Z. Panagiotopoulos, *Phys. Rev. E* **66**, 041204 (2002).
- [25] Q. Yan and J. J. de Pablo, *J. Chem. Phys.* **116**, 2967 (2002).
- [26] H. L. Friedman and H. Taube, *J. Am. Chem. Soc.* **72**, 3362 (1950).
- [27] M. L. Japas and J. M. H. L. Sengers, *J. Phys. Chem.* **94**, 5361 (1990).
- [28] R. R. Singh and K. Pitzer, *J. Chem. Phys.* **92**, 6775 (1990).
- [29] H. Weingärtner, S. Wiegand, and W. Schröer, *J. Chem. Phys.* **96**, 848 (1992).
- [30] T. Narayanan and K. Pitzer, *J. Phys. Chem.* **98**, 9170 (1994).
- [31] E. Gonzalez-Tovar, M. Lozada-Cassou, L. M. y Terán, and M. Medina-Noyola, *J. Chem. Phys.* **95**, 6784 (1991).
- [32] M. Lozada-Cassou, *J. Chem. Phys.* **75**, 1412 (1981).
- [33] M. Lozada-Cassou, *J. Chem. Phys.* **80**, 3344 (1984).
- [34] M. Lozada-Cassou and E. Díaz-Herrera, *J. Chem. Phys.* **92**, 1194 (1990).
- [35] M. Lozada-Cassou and E. Díaz-Herrera, *J. Chem. Phys.* **93**, 1386 (1990).
- [36] J. E. Sánchez and M. Lozada-Cassou, *Chem. Phys. Lett.* **190**, 202 (1992).
- [37] M. Lozada-Cassou, in *Fundamentals of inhomogeneous fluids*, edited by D. Henderson (Marcel Dekker, New York, 1993), Chap. 8.
- [38] J. Alejandre, M. Lozada-Cassou, E. González-Tovar, and G. A. Chapela, *Chem. Phys. Lett.* **172**, 111 (1990).
- [39] J. P. Valleau, R. Ivkov, and J. M. Torrie, *J. Chem. Phys.* **95**, 520 (1991).
- [40] M. Lozada-Cassou, W. Olivares, and B. Sulbarán, *Phys. Rev. E* **53**, 522 (1996).
- [41] All those theories which are derived from the Orstein-Zernike equation plus any of the established closures, we refer to as *standard* integral equations theories.

- [42] R. Kjellander and S. Marcelia, *Mol. Phys.* **83**, 789 (1994).
- [43] M. Plischke and D. Henderson, *J. Phys. Chem.* **92**, 7177 (1988).
- [44] M. Plischke and D. Henderson, *Electrochim. Acta* **34**, 1863 (1989).
- [45] P. Attard, *J. Chem. Phys.* **91**, 3072 (1989).
- [46] P. Attard, *J. Chem. Phys.* **91**, 3083 (1989).
- [47] M. E. Fisher, *J. Stat. Phys.* **75**, 1 (1994).
- [48] Y. Levin and M. E. Fisher, *Physica A* **225**, 164 (1996).
- [49] N. Bjerrum, *Kgl. Dan. Vidensk. Selsk. Mat.-Fys. Medd.* **7**, 1 (1926).
- [50] B. Hafskjold and G. Stell, in *The liquid state of matter*, edited by E. W. Montroll and J. L. Lebowitz (North Holland, New York, 1972).
- [51] G. Stell, K. C. Wu, and B. Larsen, *Phys Rev. Lett* **37**, 1369 (1976).
- [52] Y. Q. Zhou, S. Yeh, and G. Stell, *J. Chem. Phys.* **102**, 5785 (1995).
- [53] S. Yeh, Y. Q. Zhou, and G. Stell, *J. Phys. Chem.* **100**, 1415 (1996).
- [54] F. O. Raineri, J. P. Routh, and G. Stell, *J. Phys. IV* **10**, Pr5 (2000).
- [55] L. Blum and O. Bernard, *J. Stat. Phys.* **79**, 569 (1995).
- [56] O. Bernard and L. Blum, *J. Chem. Phys.* **104**, 4746 (1996).
- [57] J. W. Jiang, L. Blum, and O. Bernard, *Mol. Phys.* **99**, 1765 (2001).
- [58] J. W. Jiang *et al.*, *J. Chem. Phys.* **116**, 7977 (2002).
- [59] S. H. Suh, L. M. y Terán, and H. S. W. H. T. Davis, *J. Chem. Phys.* **142**, 203 (1990).
- [60] K. C. Zhang, M. E. Briggs, R. W. Gammon, and J. M. H. L. Sengers, *J. Chem. Phys.* **97**, 8692 (1992).
- [61] S. Wiegand *et al.*, *J. Chem. Phys.* **109**, 9038 (1998).
- [62] R. R. Singh and K. S. Pitzer, *J. Am. Chem. Soc.* **110**, 8723 (1988).
- [63] T. Narayanan and K. S. Pitzer, *Phys. Rev. Lett.* **73**, 3002 (1994).
- [64] T. Narayanan and K. S. Pitzer, *J. Chem. Phys.* **102**, 8118 (1995).
- [65] K. Gutkowski, M. A. Anisimov, and J. V. Sengers, *J. Chem. Phys.* **114**, 3133 (2001).
- [66] D. A. McQuarrie, *Statistical Mechanics* (Harper and Row, New York, 1976).
- [67] H. L. Friedman, *A Course in Statistical Mechanics* (Prentice Hall, Englewood Cliffs, NJ, 1985).
- [68] J. P. Hansen and I. R. McDonald, *Theory of simple liquids*, 2nd ed. (Academic Press, London, 1986).
- [69] M. Born and M. S. Green, *A General Kinetic Theory of Liquids* (Cambridge University Press,

- Cambridge, 1949).
- [70] J. Yvon, *La Théorie Statistique des Fluides et l'Equation d'Etat, Actualités Scientifiques et Industrielles* (Hermann, Paris, 1935), Vol. 203.
- [71] G. Arfken, *Mathematical Methods for Physicists* (Academic Press Inc., San Diego, CA, 1985).
- [72] R. Messina, C. Holm, and K. Kremer, *Phys. Rev. Lett.* **85**, 872 (2000).
- [73] R. Messina, C. Holm, and K. Kremer, *Europhys. Lett.* **51**, 461 (2000).
- [74] R. Messina, C. Holm, and K. Kremer, *Phys. Rev. E* **64**, 021405 (2001).
- [75] M. Deserno and C. Holm, *J. Chem. Phys.* **109**, 7678 (1998).
- [76] L. Degève, M. Lozada-Cassou, E. Sánchez, and E. González-Tovar, *J. Chem. Phys.* **98**, 8905 (1993).
- [77] In Fig. 4 of ref. [21] it is plotted the energy calculated by the unscreened interaction potential of four ions, and is not a simulation result [80]. In our case, our conclusions are derived from the potential of mean force. Hence aligned clusters seem to be better supported by our theory and is not in contradiction with the simulation results of Yan and de Pablo.
- [78] L. M. y Teeran, E. Díaz-Herrera, M. Lozada-Cassou, and R. Saavedra-Barrera, *J. Comp. Phys.* **84**, 326 (1989).
- [79] O. C. Zienkiewicz and R. L. Taylor, *The Finite Element Method*, 4th ed. (McGraw Hill Book Company, London, 1989), Vol. 1.
- [80] J. J. de Pablo, personal communication.

$g^{(2)}(r)$			
$n$	Exact	HNC	PY
1			
2			

FIG. 1: Mayer diagrams for the first ( $n = 1$ ) and second ( $n = 2$ ) order in  $\rho$  expansion of the pair correlation function,  $g^{(2)}(r)$ . The exact, hypernetted chain (HNC) and Percus-Yevick (PY) coefficients are shown. The black points and white dots are called field and root points, respectively. The bonds represent the Mayer function  $f(\mathbf{r}_{12})$ .

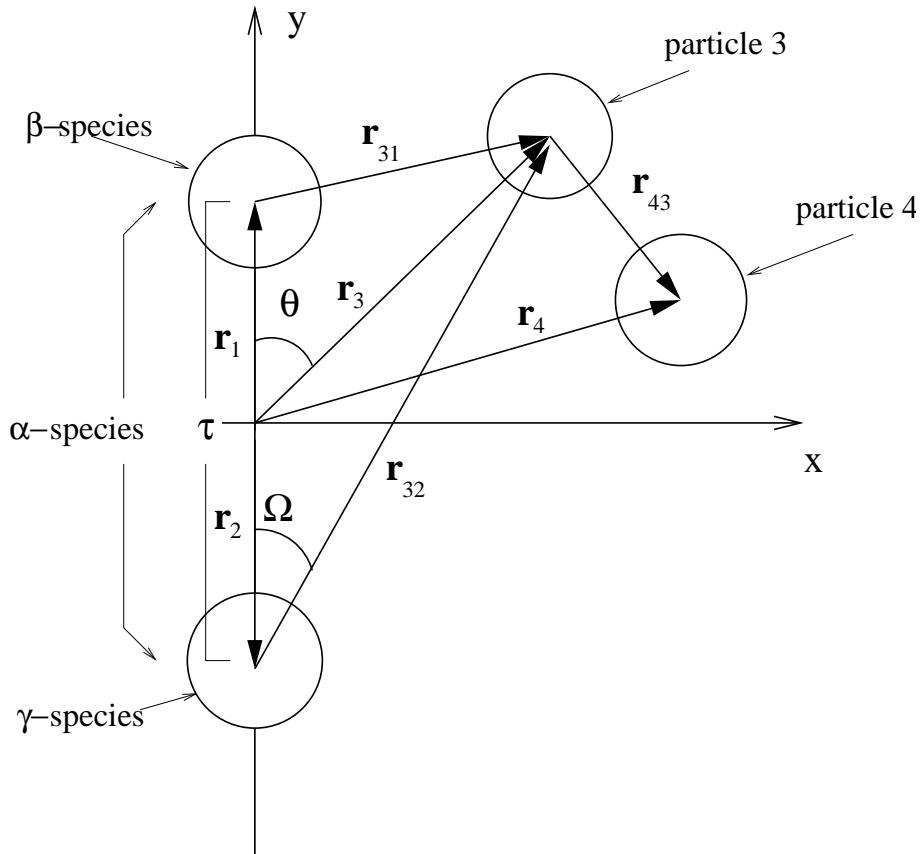


FIG. 2: Schematic representation of the model.

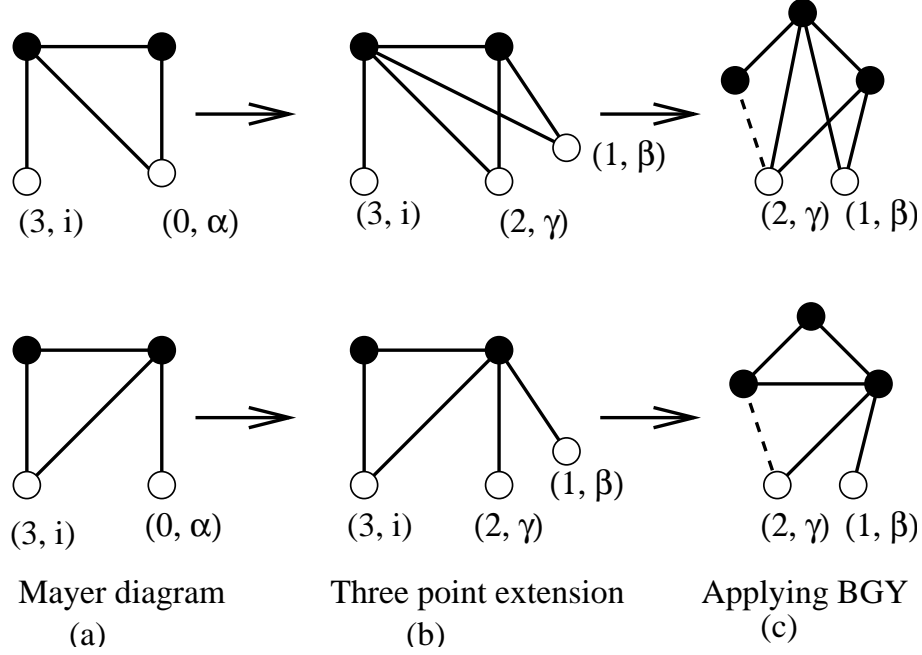


FIG. 3: Two examples of the transformation of Mayer diagrams under TPE. The notation for the particles and species is the same as in Fig. 2. The dashed bond represents the  $f_{\gamma i}(r_{23}) = \frac{du_{\gamma i}(\mathbf{r}_{23})}{dr_{23}}$  function. Thereby, in  $(N, \delta)$ ,  $N$  stands for the particle number and  $\delta$  for the particle species (see also Fig. 2).  $N = 0$  stands for the dumbbell particle. (a) An example of a second order Mayer diagram involving a dumbbell particle and particle 3. (b) The same diagram as in (a) but the constitutive particles of the dumbbell are explicited, i. e., at the level of the triplet correlation function. (c) Resulting diagrams upon applying BGY (on the level of the mean force).

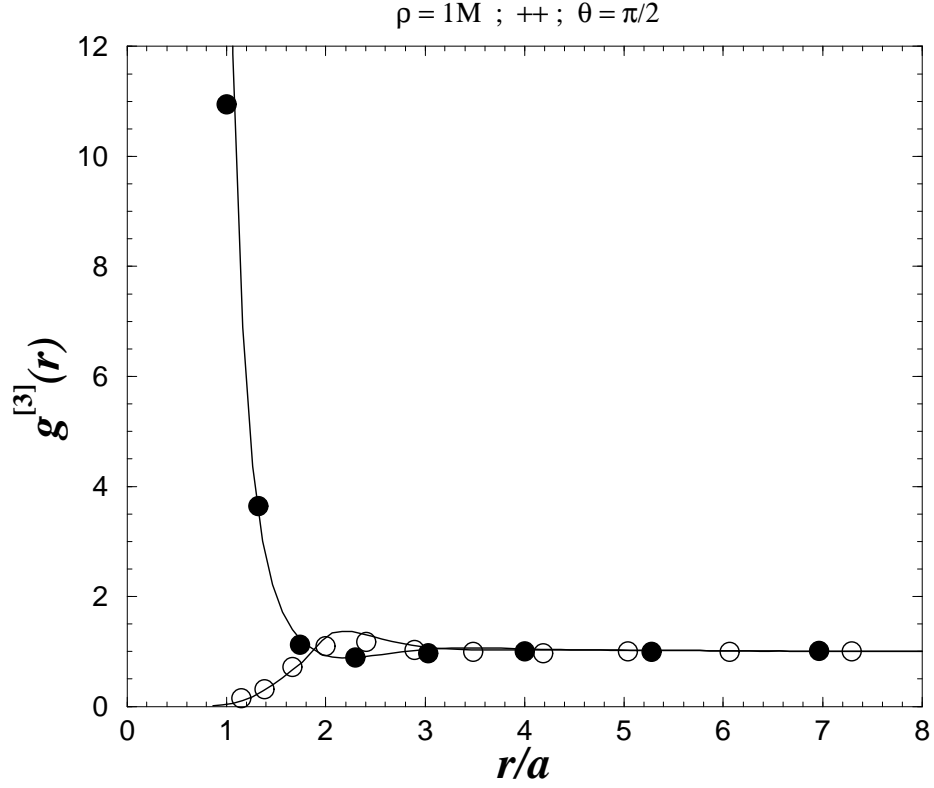


FIG. 4: Three particle distribution function  $g_{++i}^{[3]}(r, \theta = \pi/2; \tau = a)$  for a dumbbell made of two (divalent) positive particles, with  $\rho = 1M$  and  $z = 2$ . The solid lines represent the results from TPE-HNC/MSA. The MD results are shown in filled and open circles for  $g_{++-}^{[3]}(r, \pi/2; a)$  and  $g_{+++}^{[3]}(r, \pi/2; a)$  respectively.

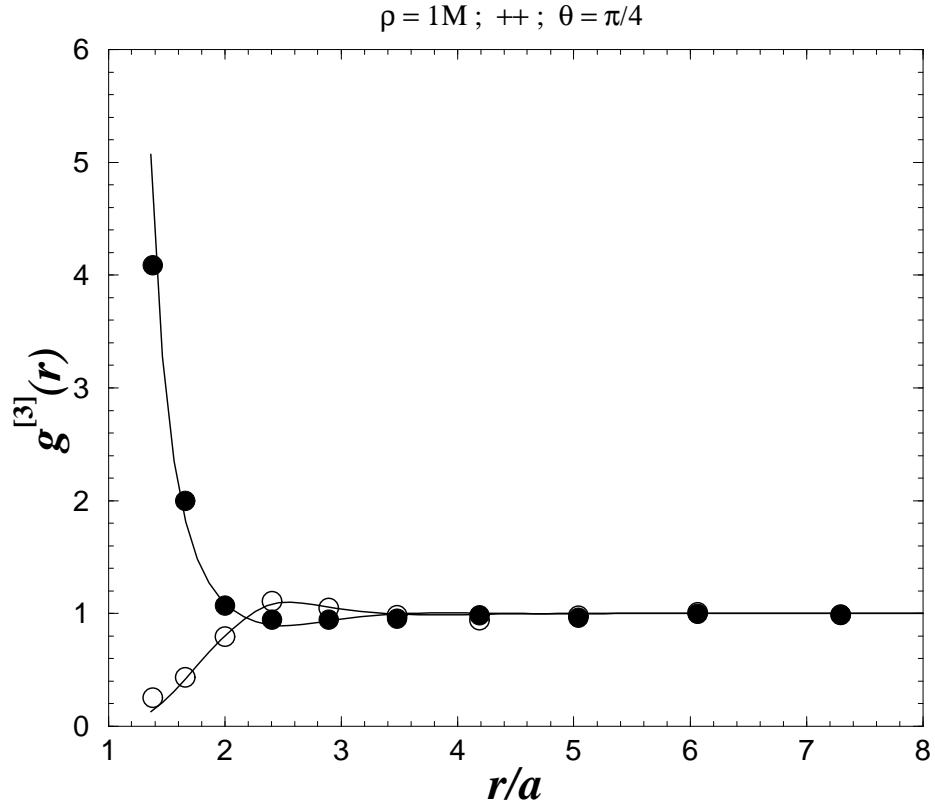


FIG. 5: Same as in Fig.4 with  $\theta = \pi/4$ .

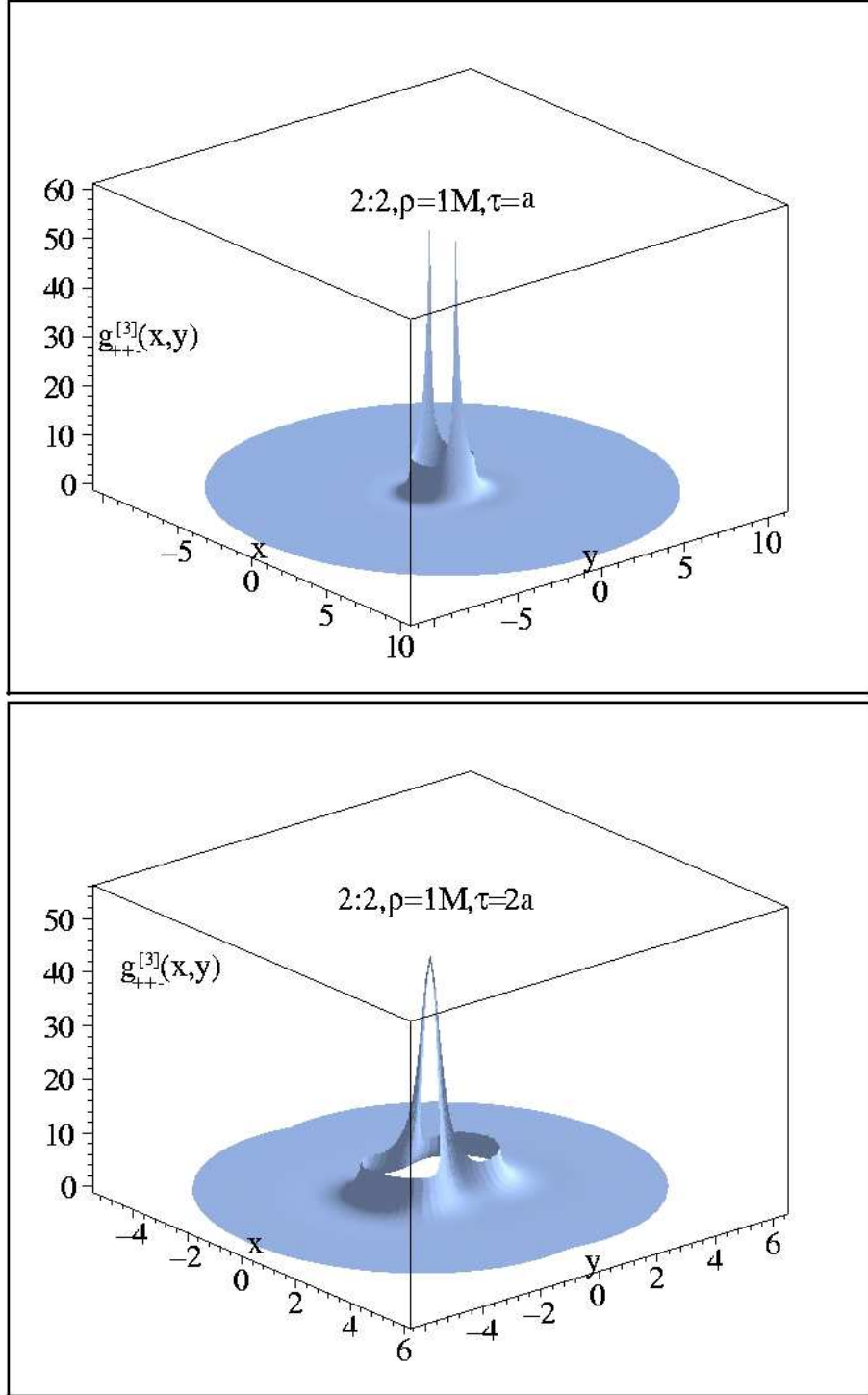


FIG. 6: 3D representation (in Cartesian coordinates) of: (a) (upper 3D plot)  $g_{+++}^{[3]}(r, \theta; \tau = a)$  and (b) (lower 3D plot)  $g_{+++}^{[3]}(r, \theta; \tau = 2a)$  obtained by TPE-HNC/MSA for the same fluid parameters as in Figs. 4 and 5. The dumbbell axis is parallel to  $y$  axis.



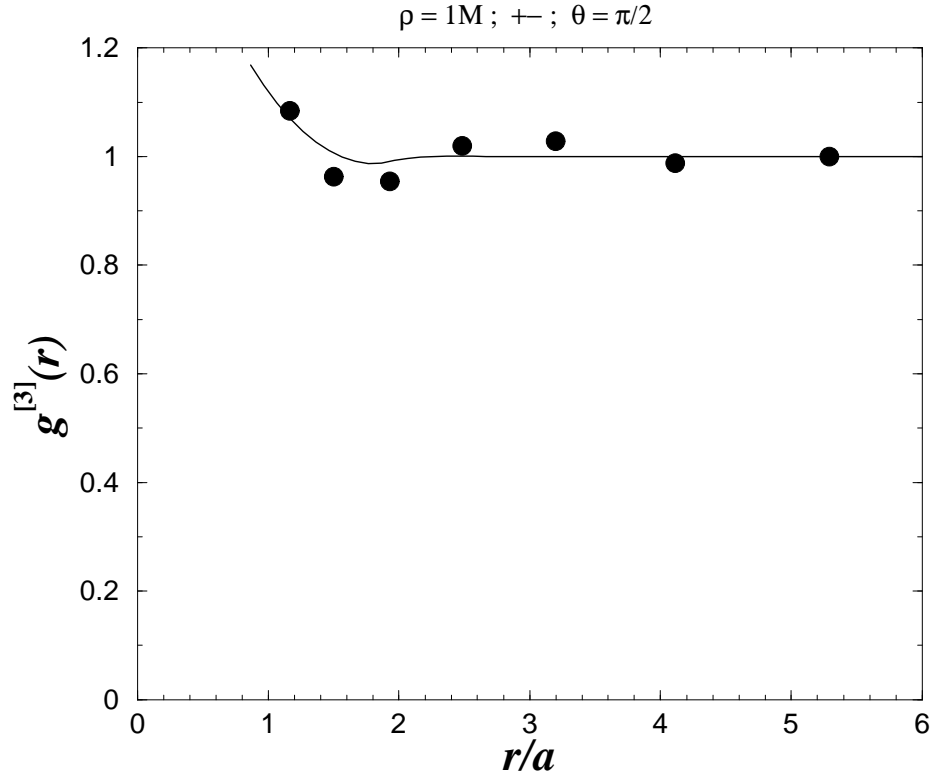


FIG. 7: Three particle distribution function  $g_{+-i}^{[3]}(r, \theta = \pi/2; \tau = a)$  for a dumbbell made of a positive and a negative divalent ions, with  $\rho = 1M$  and  $z = 2$ . The solid lines represent the results from TPE-HNC/MSA. The MD results are shown in filled circles. The curves for  $g_{+--}^{[3]}(r, \pi/2; a)$  and  $g_{+-+}^{[3]}(r, \pi/2; a)$  collapse in a single curve.

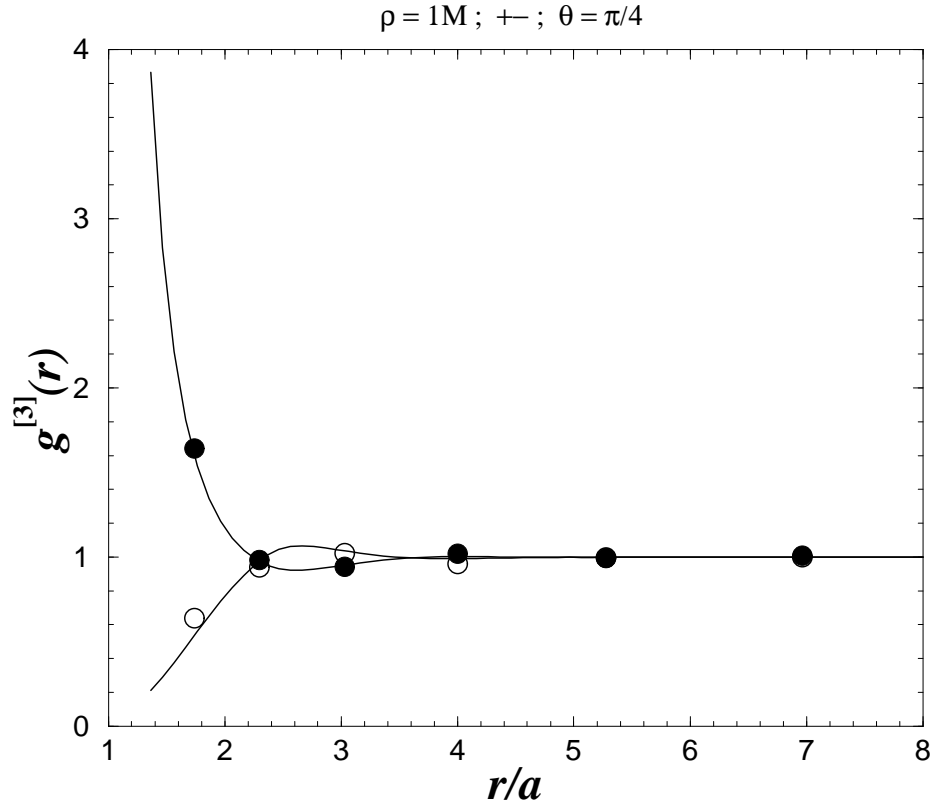


FIG. 8: Same as in Fig. 7 with  $\theta = \pi/4$ . The MD results are shown in filled and open circles for  $g_{+-}^{[3]}(r, \pi/4; a)$  and  $g_{++}^{[3]}(r, \pi/4; a)$  respectively.

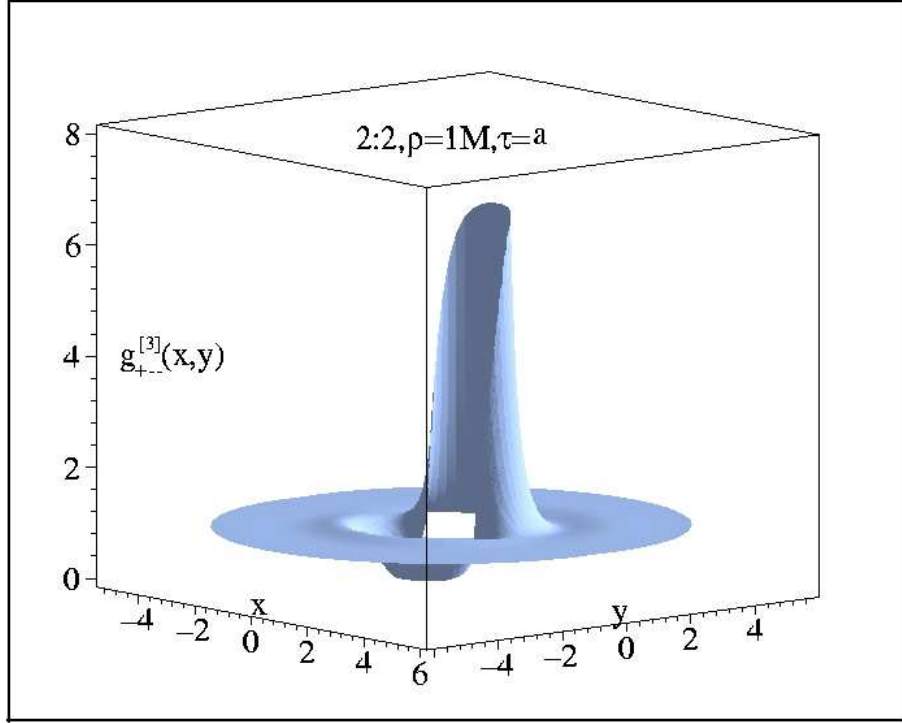


FIG. 9: 3D representation (in Cartesian coordinates) of  $g_{+-}^{[3]}(r, \theta; a)$  obtained by TPE-HNC/MSA for the same fluid parameters as in Figs.7 and 8. The dumbbell axis is parallel to  $y$  axis.

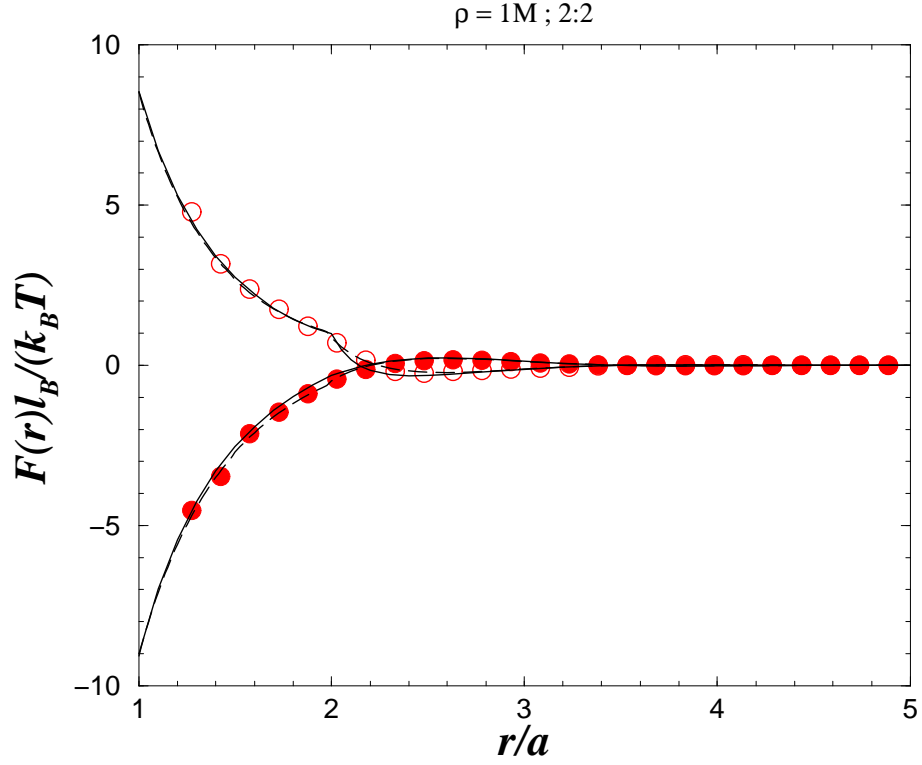


FIG. 10: Effective forces between two like charges [ $F_{++}(r) > 0$ ] and two opposite charges [ $F_{+-}(r) < 0$ ] as a function of their separation  $r$ , in reduced units of  $\frac{k_B T}{\ell_B}$ , with  $\rho = 1\text{M}$  and  $z = 2$ . The solid lines represent the results from TPE-HNC/MSA and the dashed lines are the results from HNC/MSA. The MD results are shown in filled and open circles for  $F_{+-}(r)$  and  $F_{++}(r)$ , respectively.

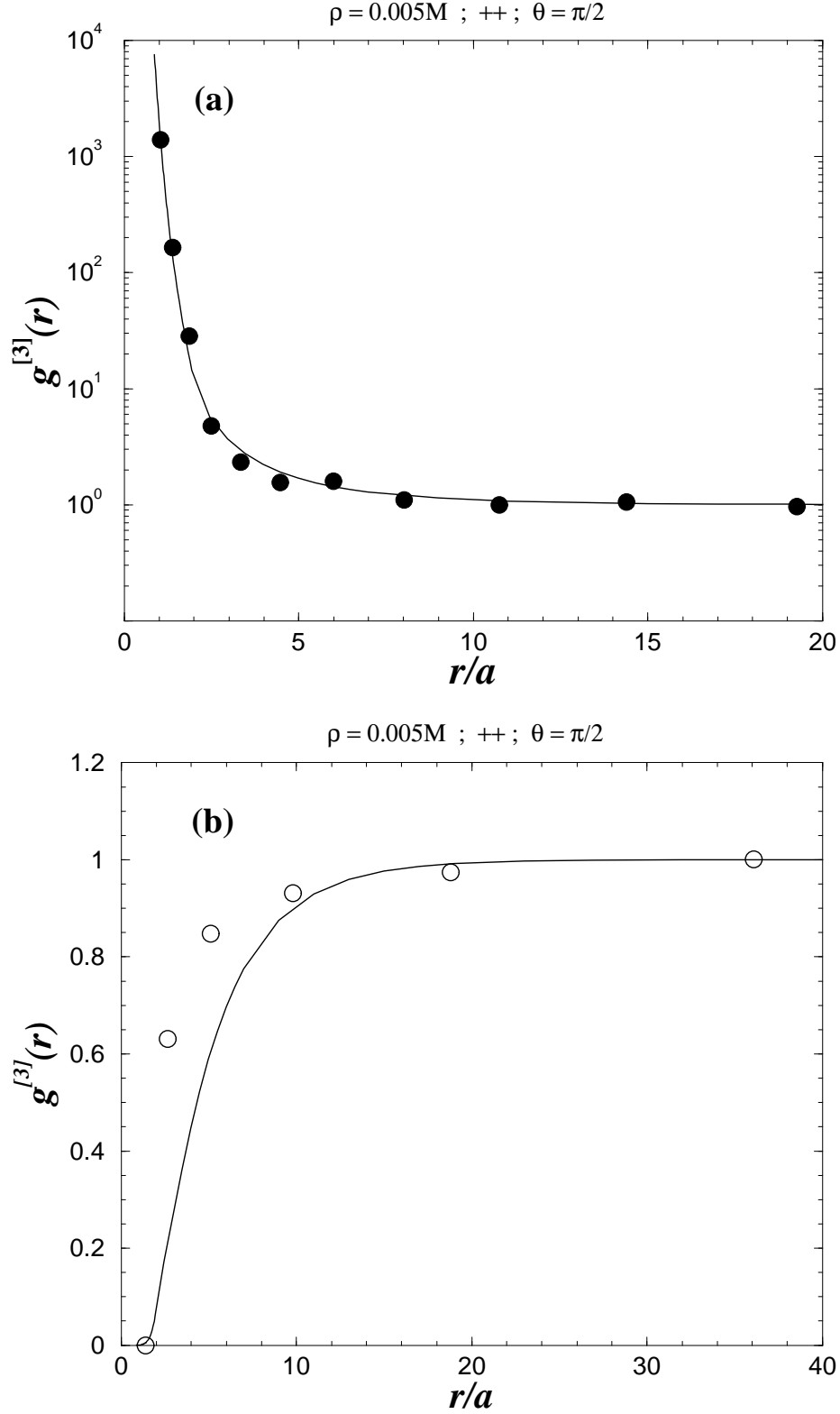


FIG. 11: Three particle distribution function with  $\rho = 0.005M$  and  $z = 2$ : (a)  $g_{+++}^{[3]}(r, \pi/2; a)$  and (b)  $g_{+--}^{[3]}(r, \pi/2; a)$ . The solid lines represent the results from TPE-HNC/MSA. The MD results are shown in filled and open circles for (a)  $g_{+++}^{[3]}(r, \pi/2; a)$  and (b)  $g_{+--}^{[3]}(r, \pi/2; a)$ , respectively.

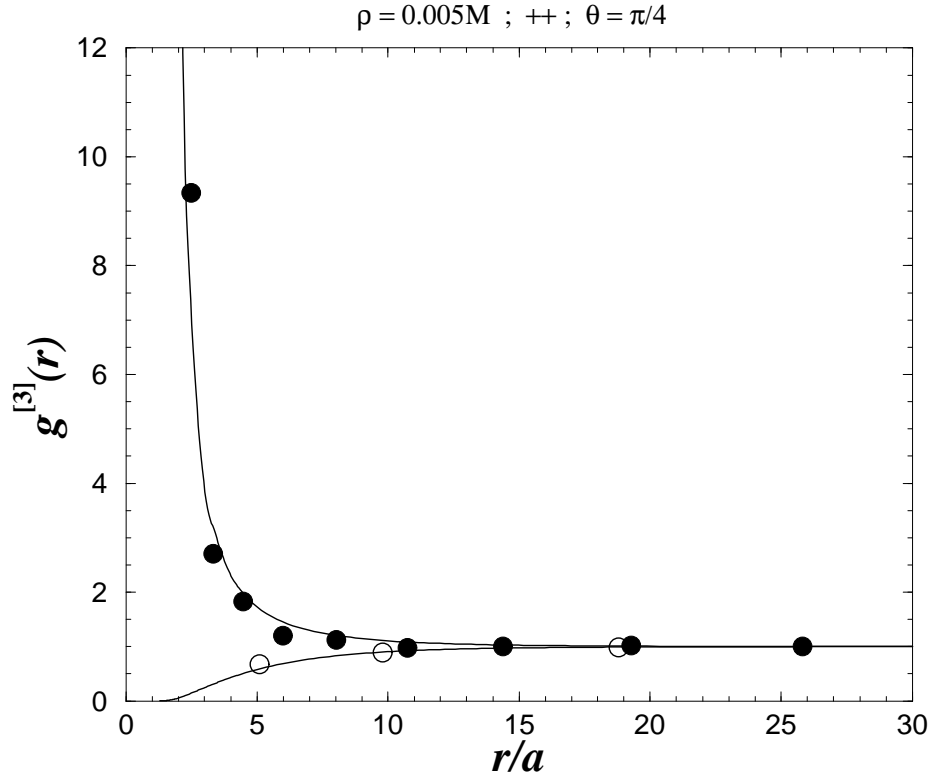


FIG. 12: Same as in Fig. 11 with  $\theta = \pi/4$ . The MD results are shown in filled and open circles for  $g_{++-}^{[3]}(r, \pi/2; a)$  and  $g_{+++}^{[3]}(r, \pi/2; a)$ , respectively.

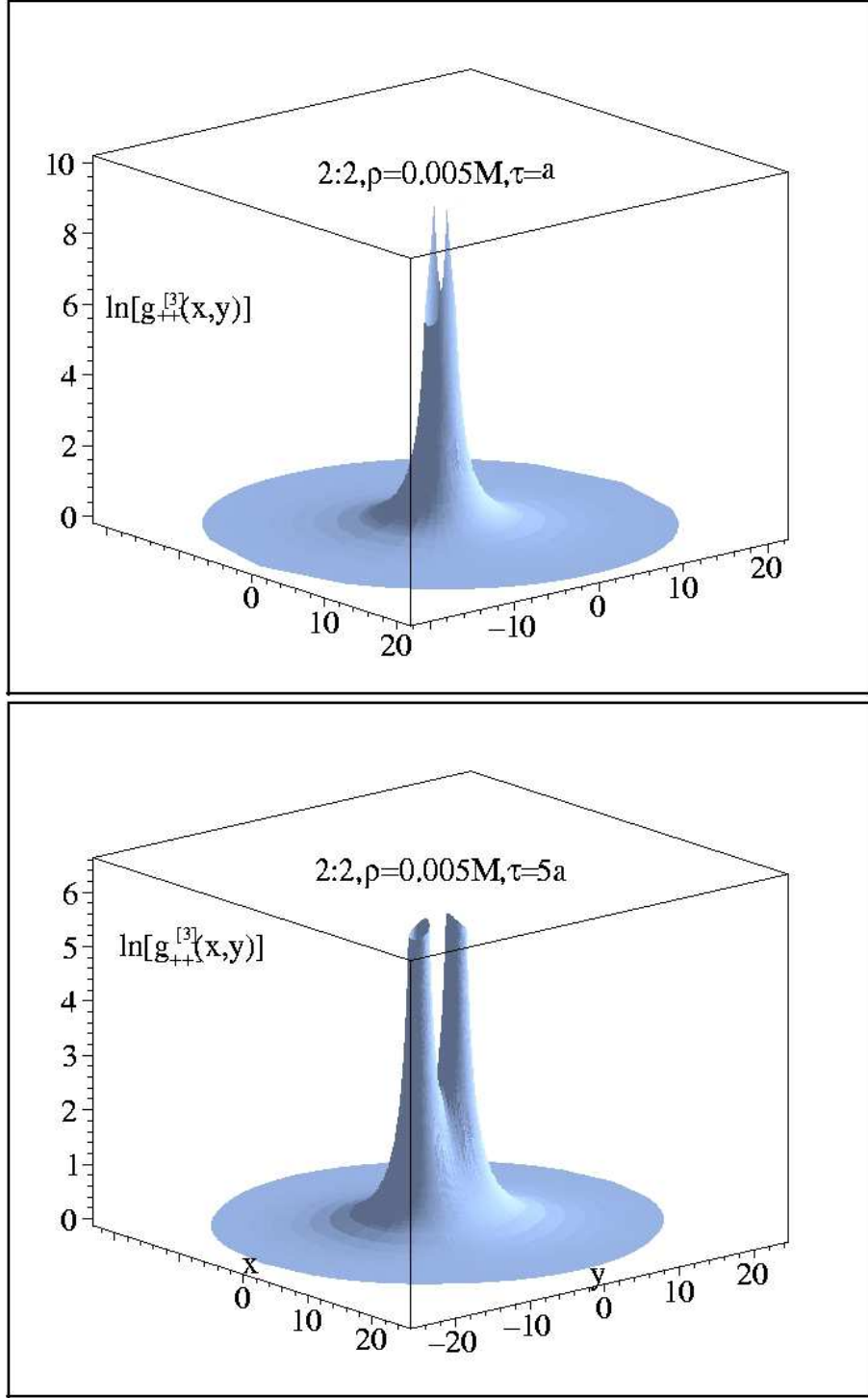


FIG. 13: 3D representation (in Cartesian coordinates) of  $g_{++}^{[3]}(r, \theta; \tau)$  obtained by TPE-HNC/MSA for the same fluid parameters as in Figs. 11 and 12. The dumbbell axis is parallel to  $y$  axis. (a)  $\tau = a$  (b)  $\tau = 5a$ .

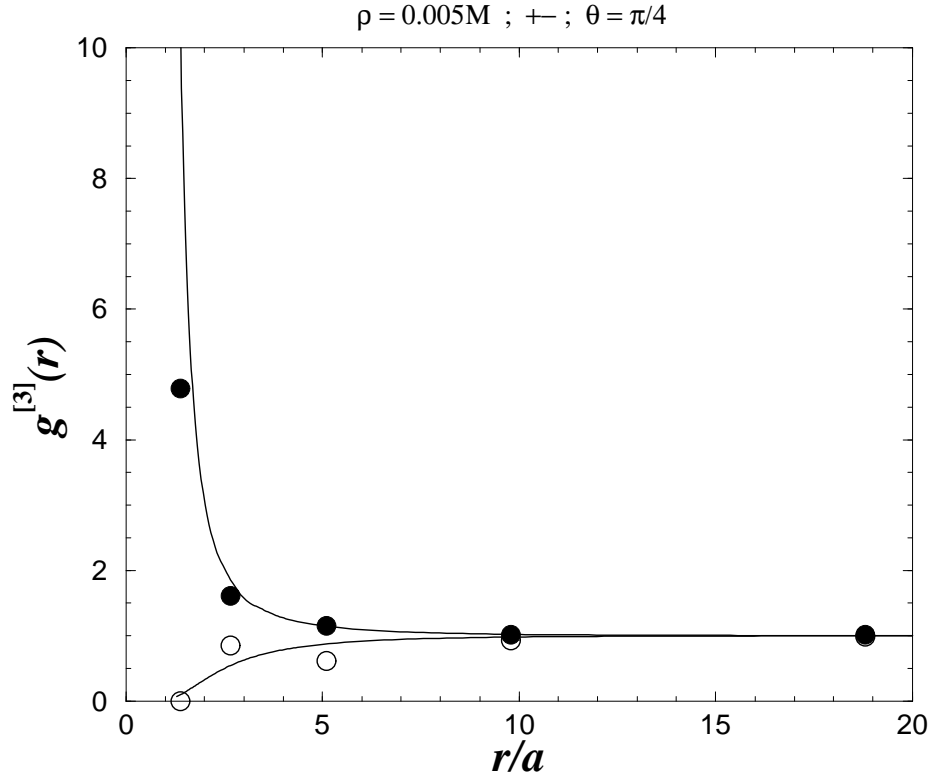


FIG. 14: Three particle distribution function  $g_{+-i}^{[3]}(r, \pi/4; a)$  with  $\rho = 0.005M$  and  $z = 2$ . The solid lines represent the results from TPE-HNC/MSA. The MD results are shown in filled and open circles for  $g_{+-i}^{[3]}(r, \pi/4; a)$  and  $g_{+--+}^{[3]}(r, \pi/4; a)$ , respectively.



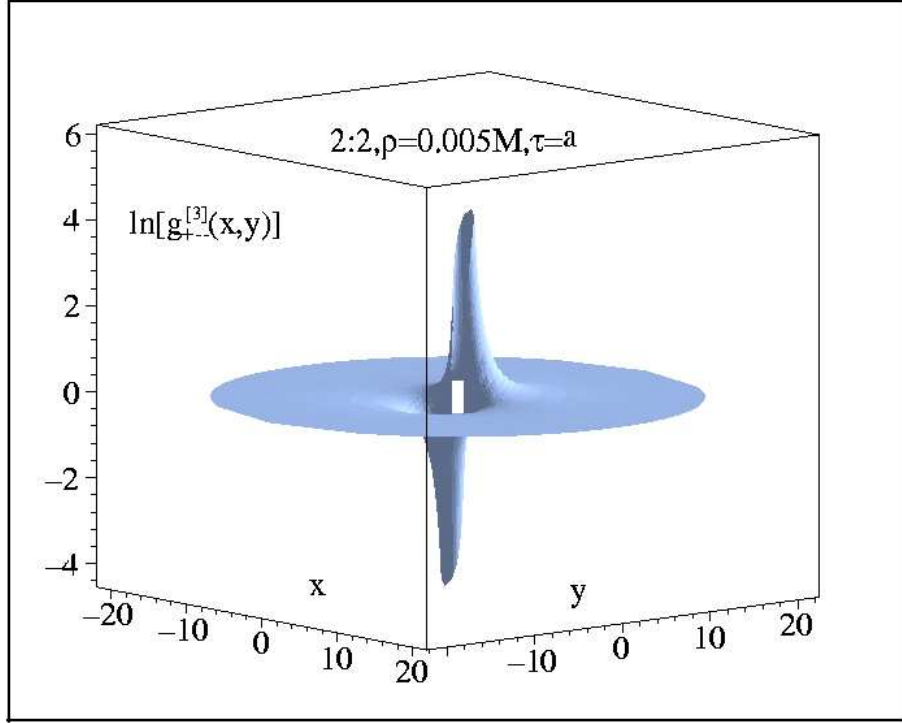


FIG. 15: 3D representation (in Cartesian coordinates) of  $g_{+-}^{[3]}(r, \theta; a)$  obtained by TPE-HNC/MSA for the same fluid parameters as in Fig. 14. The dumbbell axis is parallel to  $y$  axis.

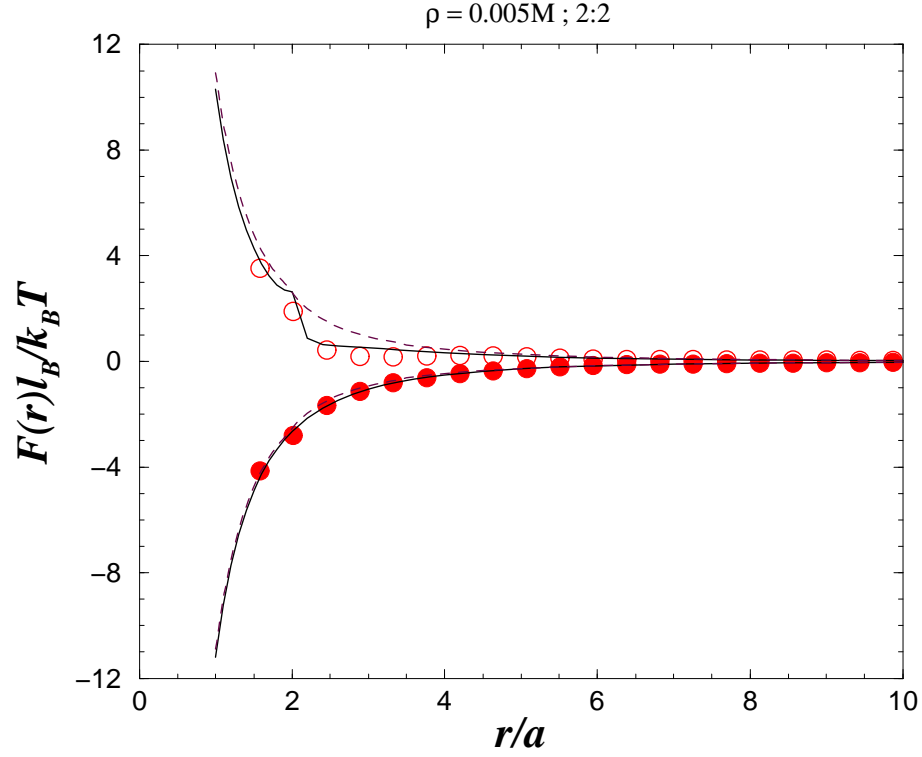


FIG. 16: Effective forces between two like charges [ $F_{++}(r) > 0$ ] and two opposite charges [ $F_{+-}(r) < 0$ ] as a function of their separation  $r$ , in reduced units of  $\frac{k_B T}{\ell_B}$ , with  $\rho = 0.005M$  and  $z = 2$ . The solid lines represent the results from TPE-HNC/MSA and the dashed lines are the results from HNC/MSA. The MD results are shown in filled and open circles for  $F_{+-}(r)$  and  $F_{++}(r)$ , respectively.

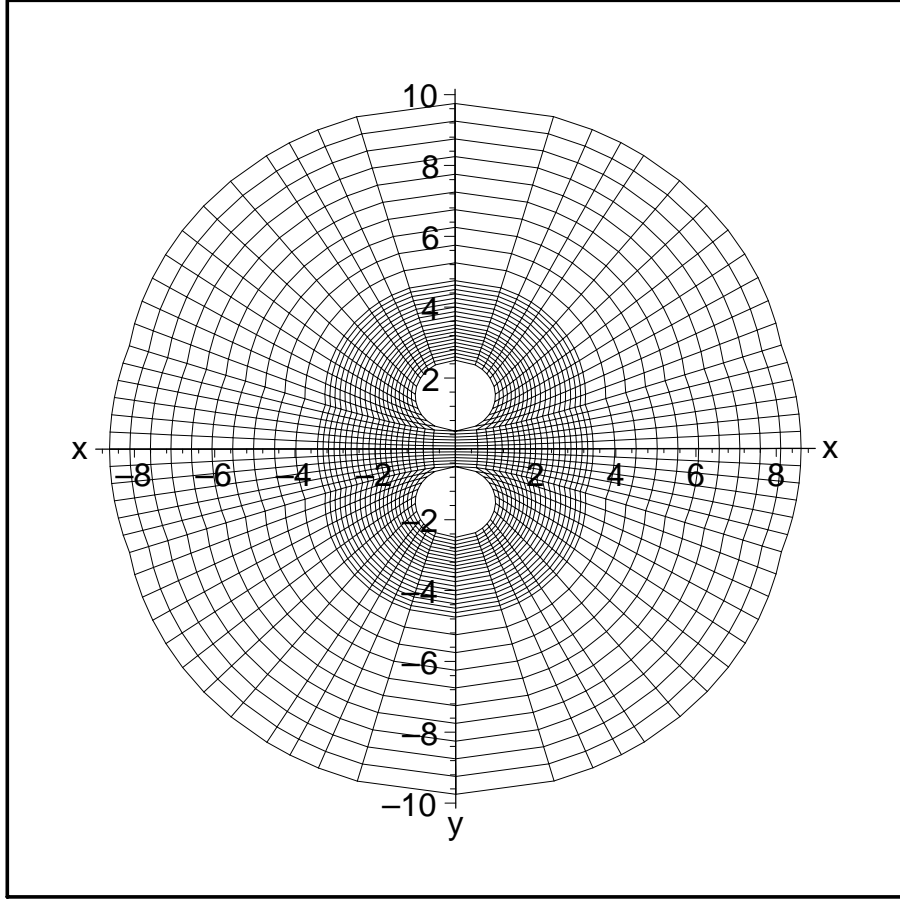


FIG. 17: An example of the grid (in Cartesian coordinates) used to solve Eq.(A1).

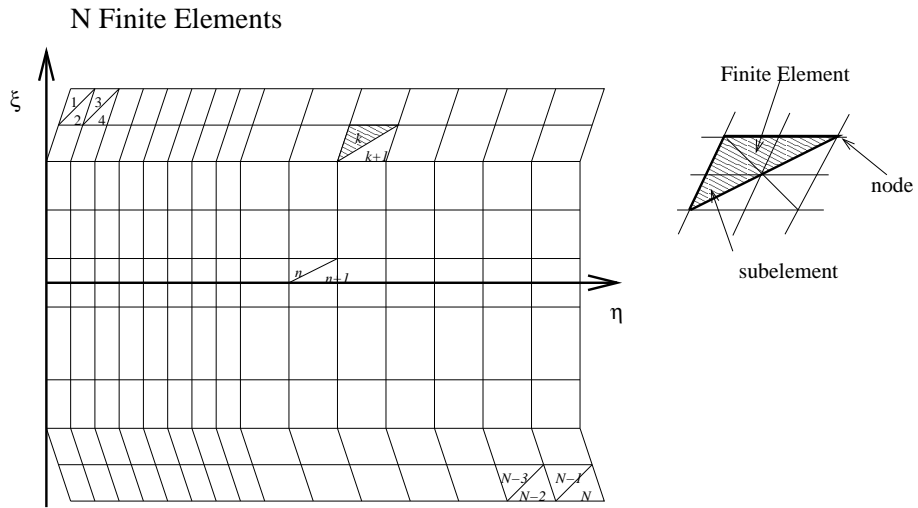


FIG. 18: The same grid as in in Fig. 17 but mapped into the  $\eta - \xi$  plane. A triangular element and its 6 nodes are represented.